# Mass Ejection from the Remnant of a Binary Neutron Star Merger: Viscous-radiation Hydrodynamics Study

Sho Fujibayashi[1] , Kenta Kiuchi[1] , Nobuya Nishimura[1] , Yuichiro Sekiguchi[1,2], and Masaru Shibata[1,3]
[1] Center for Gravitational Physics, Yukawa Institute for Theoretical Physics, Kyoto University, Kyoto 606-8502, Japan; sho.fujibayashi@yukawa.kyoto-u.ac.jp
[2] Department of Physics, Toho University, Funabashi, Chiba 274-8510, Japan
[3] Max Planck Institute for Gravitational Physics (Albert Einstein Institute), Am Mühlenberg 1, Potsdam-Golm, D-14476, Germany
Received 2017 November 9; revised 2018 February 27; accepted 2018 March 6; published 2018 June 12

Abstract

We perform long-term general relativistic neutrino radiation hydrodynamics simulations (in axisymmetry) for a massive neutron star (MNS) surrounded by a torus, which is a canonical remnant formed after the binary neutron star merger. We take into account the effects of viscosity, which is likely to arise in the merger remnant due to magnetohydrodynamical turbulence. The viscous effect plays key roles for the mass ejection from the remnant in two phases of the evolution. In the first $t \lesssim 10$ ms, a differential rotation state of the MNS is changed to a rigidly rotating state. A shock wave caused by the variation of its quasi-equilibrium state induces significant mass ejection of mass $\sim(0.5\text{–}2.0) \times 10^{-2} M_\odot$ for the α-viscosity parameter of 0.01–0.04. For the longer-term evolution with $\sim$0.1–10 s, a significant fraction of the torus material is ejected. We find that the total mass of the viscosity-driven ejecta ($\gtrsim 10^{-2} M_\odot$) could dominate over that of the dynamical ejecta ($\lesssim 10^{-2} M_\odot$). The electron fraction, Y_e, of the ejecta is always high enough ($Y_e \gtrsim 0.25$) that this post-merger ejecta is lanthanide-poor; hence, the opacity of the ejecta is likely to be $\sim$10–100 times lower than that of the dynamical ejecta. This indicates that the electromagnetic signal from the ejecta would be rapidly evolving, bright, and blue if it is observed from a small viewing angle ($\lesssim 45°$) for which the effect of the dynamical ejecta is minor.

Key words: accretion, accretion disks – neutrinos – relativistic processes – stars: neutron

1. Introduction

The merger of binary neutron stars is one of the most promising gravitational-wave sources for ground-based detectors such as advanced LIGO (Abadie et al. 2010), advanced VIRGO (Accadia et al. 2011), and KAGRA (Kuroda & LCGT Collaboration 2010). Gravitational waves from binary neutron stars carry information on the mass and tidal deformability of neutron stars. The total mass and mass ratio will be used for exploring the formation process of binary neutron stars (Tauris et al. 2017). The tidal deformability together with the mass will give us invaluable information for exploring the properties of the high-density nuclear matter (Flanagan & Hinderer 2008). The latest detection of gravitational waves from a system of binary neutron stars, GW170817, indeed shows that the detection will give us such information on neutron stars (Abbott et al. 2017a).

Associated with gravitational waves, a variety of electromagnetic signals are likely to be emitted, because an appreciable amount of mass is likely to be ejected from the system with high velocity (10%–30% of the speed of light) during the merger and post-merger phases (e.g., Dessart et al. 2009; Bauswein et al. 2013; Fernández & Metzger 2013; Hotokezaka et al. 2013b; Rosswog 2013; Metzger & Fernández 2014; Perego et al. 2014; Foucart et al. 2015, 2016; Just et al. 2015; Sekiguchi et al. 2015; Radice et al. 2016). One promising scenario for the electromagnetic emission is described by the so-called macronova/kilonova model (Li & Paczyński 1998; Metzger et al. 2010). In this model, a fraction of neutron-rich matter of mass $\sim$0.01–0.1 $M_\odot$ is ejected from the merger event, then the *r*-process nucleosynthesis proceeds in the ejecta for synthesizing a variety of neutron-rich heavy nuclei (Lattimer & Schramm 1974; Symbalisty & Schramm 1982; Eichler et al. 1989;

Freiburghaus et al. 1999; Goriely et al. 2011; Wanajo et al. 2014; Just et al. 2015; Martin et al. 2015; Lippuner et al. 2017). By the continuous radioactive decay of the *r*-process elements, the ejecta is heated up. For the early phase of its expansion, the ejecta is so dense that it is optically thick to photons. Thus, the generated heat is consumed by the adiabatic expansion in this phase. However, when the density of the matter becomes low enough for photons to diffuse out in a timescale shorter than the expansion timescale, the ejecta starts shining brightly. According to the macronova/kilonova model, the time to reach peak emission is $\sim$1–10 days after the merger, and the luminosity at the peak is $\sim 10^{41}$–10^{42} erg s^{-1} in the optical to infrared bands, depending on the mass, velocity, and opacity of the ejecta (Metzger et al. 2010). Such electromagnetic signals consistent with macronova/kilonova were indeed observed simultaneously with GW170817 (e.g., Abbott et al. 2017b; Arcavi et al. 2017; Coulter et al. 2017; Cowperthwaite et al. 2017; Drout et al. 2017; Kasliwal et al. 2017; Nicholl et al. 2017; Pian et al. 2017; Shappee et al. 2017; Smartt et al. 2017; Soares-Santos et al. 2017; Tanaka et al. 2017).

For extracting the information of the merger process from the observed electromagnetic signals, we need reliable theoretical modeling for the mass ejection and resulting electromagnetic emission. For this purpose, numerical-relativity simulation taking into account a variety of physical ingredients, such as neutrino emission and absorption, angular momentum transport, and equation of state (EOS) for the neutron star matter, is the unique approach.

In this paper, we focus on the evolution of a remnant of a binary neutron star merger. As found in our previous works (e.g., Hotokezaka et al. 2013a; Sekiguchi et al. 2015, 2016), after the merger of binary neutron stars with a typical total mass 2.6–2.8 $M_\odot$, a massive neutron star (MNS)

surrounded by a dense torus of mass 0.2–0.3 $M_\odot$ is formed as a typical remnant. Such remnants are always differentially and rapidly rotating and, furthermore, are likely to be highly magnetized, possibly in a magnetohydrodynamic (MHD) turbulence state (Kiuchi et al. 2015b, 2017). As a result, the turbulent viscosity is likely to arise effectively. In addition, the remnant is so hot that it emits a huge amount of neutrinos. Consequently, the neutrino irradiation process would change the electron fraction of the matter in the envelope and ejecta and influence the feature of the observational signals significantly because the electron fraction is closely related to the efficiency for synthesizing lanthanide elements, which are the major players for enhancing the opacity of the ejecta (Kasen et al. 2013; Tanaka & Hotokezaka 2013; Kasen et al. 2015; Tanaka et al. 2018).

Motivated by this consideration, we perform radiation-viscous hydrodynamics simulations for a remnant of a binary neutron star merger. Following Fujibayashi et al. (2017), we first perform a radiation hydrodynamics simulation in numerical relativity for a merger of binary neutron stars of equal mass (Sekiguchi et al. 2015). We then evolve the remnant MNS surrounded by a torus by radiation-viscous hydrodynamics simulations in axisymmetric numerical relativity. We use a general relativistic viscous hydrodynamics code based on a formalism developed by Israel & Stewart (1979). The assumption of the axisymmetry is justified because the central part of the remnant relaxes to an approximately axisymmetric state in tens of ms after the onset of the merger for the equal-mass system. Assuming the axisymmetry, we can save computational costs and follow the long-term evolution of the remnant for more than a few seconds. We note that we still need about 70,000 CPU hours for simulating one model for 2 s in our axisymmetric simulations (in our computational resources, it takes about 2 months to finish each simulation).

The paper is organized as follows. In Section 2, we briefly describe our method of simulation. Then, the results of the simulation are shown in Section 3. In Section 4, we discuss the properties of the ejecta and resulting electromagnetic counterparts. Finally, we summarize this paper in Section 5. Throughout this paper, we employ the geometrical units in which $c = 1 = G$, where c and G are the speed of light and gravitational constant, respectively. In some cases, we explicitly use c and G to clarify the physical units.

2. Method

We developed a fully general relativistic, neutrino-radiation-viscous hydrodynamics code. In this code, the neutrino radiation transfer equation and Einstein's equation are solved with the same methods as those in our previous work (Fujibayashi et al. 2017), and the viscous effect is incorporated using a simplified version of the Israel–Stewart formalism (Israel & Stewart 1979) following Shibata et al. (2017b). In this section, we briefly describe the basic equations, particularly focusing on viscous hydrodynamics.

2.1. Einstein's Equation

In our code, Einstein's equation is solved using a version of the Baumgarte–Shapiro–Shibata–Nakamura puncture formalism (Shibata & Nakamura 1995; Baumgarte & Shapiro 1999; Baker et al. 2006; Campanelli et al. 2006). The quantities we evolve in our formalism (in the Cartesian coordinate basis) are

Table 1
List of the Quantities that We Evolve in Our Baumgarte–Shapiro–Shibata–Nakamura Puncture Formulation

Notation	Definition
$\tilde{\gamma}_{ij} = \gamma^{-1/3}\gamma_{ij}$	Conformal three-metric
$W = \gamma^{-1/6}$	Conformal factor
$K = \gamma^{ij}K_{ij}$	Trace of the extrinsic curvature K_{ij}
$\tilde{A}_{ij} = \gamma^{-1/3}(K_{ij} - \gamma_{ij}K/3)$	Trace-free part of K_{ij}
$F_i = \delta^{jk}\partial_j\tilde{\gamma}_{ki}$	Auxiliary variable

listed in Table 1. Here, from the spacetime metric $g_{\alpha\beta}$ and the time-like unit vector normal to spatial hypersurfaces n_α, we define the induced spatial metric as $\gamma_{\alpha\beta} \equiv g_{\alpha\beta} + n_\alpha n_\beta$. In addition, we define the determinant of the induced metric as $\gamma = \det(\gamma_{ij})$ and the extrinsic curvature as $K_{\alpha\beta} = -(1/2)\mathcal{L}_n\gamma_{\alpha\beta}$, where $\mathcal{L}_n$ is the Lie derivative with respect to n^α. For the gauge conditions, we employ dynamical lapse and shift gauge conditions that are the same as Equations (1) and (2) in Fujibayashi et al. (2017). We adopt the so-called cartoon method (Alcubierre et al. 2001; Shibata 2003) to impose axisymmetric conditions for the geometric quantities.

2.2. Radiation-viscous Hydrodynamics Equations

As in Fujibayashi et al. (2017), we decompose neutrinos into "streaming" and "trapped" components and write the total energy-momentum tensor of the matter (fluid and neutrinos) as

$$T^{\alpha\beta}_{\mathrm{(tot)}} = T^{\alpha\beta} + \sum_i T^{\alpha\beta}_{(\nu_i,\mathrm{S})}, \tag{1}$$

where $T^{\alpha\beta} = T^{\alpha\beta}_{\mathrm{(fluid)}} + \sum_i T^{\alpha\beta}_{(\nu_i,T)}$ is the energy-momentum tensor composed of the sum of the fluid and trapped neutrinos, and $T^{\alpha\beta}_{(\nu_i,\mathrm{S})}$ denotes the energy-momentum tensor for free-streaming neutrinos. These energy-momentum tensors obey the following equations:

$$\nabla_\beta T^{\alpha\beta} = -Q^\alpha_{\mathrm{(leak)}} = -\sum_i Q^\alpha_{\mathrm{(leak)}\nu_i}, \tag{2}$$

$$\nabla_\beta T^{\alpha\beta}_{(\nu_i,\mathrm{S})} = Q^\alpha_{\mathrm{(leak)}\nu_i}, \tag{3}$$

where $Q^\alpha_{\mathrm{(leak)}\nu_i}$ denotes the leakage rate of ith species of neutrinos. For solving the evolution equations for free-streaming neutrinos, we employ the so-called M1 scheme with a closure relation (Shibata et al. 2011), and, for trapped neutrinos, we employ a leakage-based scheme developed by Sekiguchi (2010). The detailed description of these schemes is found in Sekiguchi (2010) and Fujibayashi et al. (2017).

Then, we describe the basic equations for viscous hydrodynamics. The formulation of our general relativistic viscous hydrodynamics is described in Shibata et al. (2017b) and Shibata & Kiuchi (2017). In the following, we briefly outline our formulation.

The energy-momentum tensor of the viscous fluid with trapped neutrinos is given as

$$T_{\alpha\beta} = \rho h u_\alpha u_\beta + P g_{\alpha\beta} - \rho h \nu \tau^0_{\alpha\beta}, \tag{4}$$

where ρ is the baryon rest-mass density, $h = 1 + \epsilon + P/\rho$ is the specific enthalpy, ϵ is the specific internal energy, u^α is the fluid four-velocity, P is the pressure, ν is the viscosity coefficient, and $\tau^0_{\alpha\beta}$ is the viscous stress tensor. Here $\tau^0_{\alpha\beta}$ is a

symmetric tensor that satisfies the relation $\tau^0_{\alpha\beta}u^\alpha = 0$, and, in the formalism of Israel & Stewart (1979), it obeys the evolution equation

$$\mathcal{L}_u \tau^0{}_{\alpha\beta} = -\zeta(\tau^0{}_{\alpha\beta} - \sigma_{\alpha\beta}), \tag{5}$$

where $\sigma_{\alpha\beta}$ is the shear tenor defined by

$$\sigma_{\alpha\beta} = h_\alpha{}^\mu h_\beta{}^\nu (\nabla_\mu u_\nu + \nabla_\nu u_\mu) = \mathcal{L}_u h_{\alpha\beta}, \tag{6}$$

and $h_{\alpha\beta} = g_{\alpha\beta} + u_\alpha u_\beta$. Here ζ is a nonzero constant of $(\text{time})^{-1}$ dimension, and it has to be chosen in an appropriate manner for $\tau^0_{\alpha\beta}$ to approach $\sigma_{\alpha\beta}$ in a short timescale because it is reasonable to suppose that $\tau^0_{\alpha\beta}$ should approach $\sigma_{\alpha\beta}$ in a microscopic timescale.

We can rewrite Equation (5) as

$$\mathcal{L}_u \tau_{\alpha\beta} = -\zeta \tau^0{}_{\alpha\beta}, \tag{7}$$

where $\tau_{\alpha\beta} \equiv \tau^0{}_{\alpha\beta} - \zeta h_{\alpha\beta}$. Thus, in addition to hydrodynamics equations, we solve Equation (7) as a basic equation that describes the evolution of $\tau_{\alpha\beta}$.

The energy-momentum tensor of the fluid is rewritten as

$$\begin{aligned} T_{\alpha\beta} &= \rho h (1 - \nu\zeta) u_\alpha u_\beta + (P - \rho h \nu \zeta) g_{\alpha\beta} - \rho h \nu \tau_{\alpha\beta} \\ &= \rho w \hat{e} n_\alpha n_\beta + J_\alpha n_\beta + J_\beta n_\alpha + S_{\alpha\beta}, \end{aligned} \tag{8}$$

where we defined

$$\begin{aligned} \hat{e} &\equiv T_{\alpha\beta} n^\alpha n^\beta / \rho w \\ &= hw(1 - \nu\zeta) - \frac{P - \rho h \nu \zeta}{\rho w} - h\nu w^{-3} \tau_{ij} V^i V^j, \end{aligned} \tag{9}$$

$$\begin{aligned} J_i &\equiv -T_{\alpha\beta} n^\alpha \gamma_i{}^\beta \\ &= \rho h w u_i (1 - \nu\zeta) - \rho h \nu w^{-1} \tau_{ij} V^j, \end{aligned} \tag{10}$$

$$\begin{aligned} S_{ij} &\equiv T_{\alpha\beta} \gamma^\alpha{}_i \gamma^\beta{}_j \\ &= \rho h (1 - \nu\zeta) u_i u_j + (P - \rho h \nu \zeta) \gamma_{ij} - \rho h \nu \tau_{ij}. \end{aligned} \tag{11}$$

Here $w \equiv -n_\alpha u^\alpha$ (the Lorentz factor of the fluid), and $V^i \equiv \gamma^{ij} u_j$. The general relativistic Navier–Stokes and energy equations are derived, respectively, from the space-like and time-like components of Equation (2), i.e., $\gamma_{i\alpha} \nabla_\beta T^{\alpha\beta} = -\gamma_{i\alpha} Q^\alpha_{(\text{leak})}$ and $n_\alpha \nabla_\beta T^{\alpha\beta} = -n_\alpha Q^\alpha_{(\text{leak})}$, as

$$\begin{aligned} &\partial_t(\sqrt{\gamma} J_i) + \partial_k[\sqrt{\gamma}(\alpha S^k{}_i - \beta^k J_i)] \\ &= \sqrt{\gamma}\left(-\rho_* \hat{e} \partial_i \alpha + J_k \partial_i \beta^k - \frac{\alpha}{2} S_{kl} \partial_i \gamma^{kl} - \gamma_{i\alpha} Q^\alpha_{(\text{leak})}\right), \end{aligned} \tag{12}$$

$$\begin{aligned} &\partial_t(\rho_* \hat{e}) + \partial_k[\sqrt{\gamma}(\alpha J^k - \beta^k \rho_* \hat{e})] \\ &= \sqrt{\gamma}(S_{kl} K^{kl} - \gamma^{kl} J_k \partial_l \alpha + n_\alpha Q^\alpha_{(\text{leak})}), \end{aligned} \tag{13}$$

where $\rho_* \equiv \rho w \sqrt{\gamma}$, and α and β^k denote the lapse function and shift vector, respectively. On the other hand, the evolution equation of τ_{ij} is derived from Equation (7) as

$$\begin{aligned} &\partial_t(\rho_* \tau_{ij}) + \partial_k(\rho_* \tau_{ij} v^k) \\ &= -\rho_*(\tau_{ik} \partial_j v^k + \tau_{jk} \partial_i v^k) - \rho_* \alpha w^{-1} \zeta \tau^0{}_{ij}, \end{aligned} \tag{14}$$

where we used the equation of continuity $\partial_t \rho_* + \partial_k(\rho_* v^k) = 0$ and $v^k \equiv u^k/u^t$. We solve these equations in cylindrical coordinates as in Shibata et al. (2017b).

2.3. Microphysics

For the neutron star EOS, we employ a tabulated EOS referred to as DD2 (Banik et al. 2014). We extend this EOS to low-temperature and low-density ranges down to 10^{-3} MeV and ≈ 0.1 g cm^{-3} using an EOS by Timmes & Swesty (2000) as in our previous work (Fujibayashi et al. 2017). This extended DD2 EOS includes contributions of nucleons, heavy nuclei, electrons, positrons, and photons to the pressure and internal energy.

In our formalism (Sekiguchi 2010; Fujibayashi et al. 2017), we solve the equation for the energy-momentum density of streaming neutrinos and number density of electrons and trapped neutrinos. For the source terms of these, we take into account the relevant processes due to the weak interaction. For (anti)neutrino production processes, we adopt the electron and positron capture of nucleons and heavy nuclei, electron–positron pair annihilation, nucleon–nucleon bremsstrahlung, and plasmon decay based on Fuller et al. (1985), Cooperstein et al. (1986), Burrows et al. (2006), and Ruffert et al. (1996), respectively. On the other hand, for (anti)neutrino absorption processes, we adopt the absorption of neutrinos and antineutrinos on nucleons and heavy nuclei and neutrino–antineutrino pair annihilation to electron–positron pairs. The detailed description of calculating the rates is also found in Fujibayashi et al. (2017).

Since we use the energy-integrated formalism for neutrino radiation transfer, we have to assume the average energy of neutrinos for calculating the rates of neutrino absorption and neutrino pair-annihilation processes, which depend strongly on the energy of neutrinos. In Fujibayashi et al. (2017), we found that the results of the simulation, such as the ejecta mass and kinetic energy, depend weakly on the assumption for the average neutrino energy. In this work, we adopt the average energy estimated by Equation (41) in Fujibayashi et al. (2017) because it can be derived directly from the energy integration of the energy-dependent neutrino absorption heating rate.

2.4. Prescription of the Viscosity Coefficient

In this work, we model the dynamical shear viscosity coefficient following Shakura & Sunyaev (1973) as

$$\nu = \alpha_{\text{vis}} c_s H_{\text{tur}}, \tag{15}$$

where α_{vis} is the so-called α-viscosity parameter, c_s is the sound speed, and H_{tur} is the possible largest scale of eddies in a turbulence state. In this work, we set $H_{\text{tur}} = 10$ km, because it should be approximately equal to the size of the MNS (for the central region of the system).

As already mentioned in the previous subsection, ζ^{-1} has to be a timescale short enough that $\tau^0_{\alpha\beta}$ quickly approaches $\sigma_{\alpha\beta}$. In this work, we set $\zeta = 3 \times 10^4$ s^{-1}. This value is about 4 times larger than the maximum angular velocity of the system ($\Omega \sim 8000$ rad s^{-1}); thus, the requirement for ζ is reasonably satisfied.

We note that for the outer part of the torus, the viscosity coefficient would be underestimated because the scale height of the torus increases with the radius in general. Thus, in our prescription, we conservatively take into account the effect of the viscosity for large radii.

Table 2
List of the Simulation Models

Model		α_{vis}	Δx_0 (m)	N	L (km)
DD2-135135-0.00-H		0.00	150	951	5440
DD2-135135-0.01-H		0.01	150	951	5440
DD2-135135-0.02-H	(fiducial, high)	0.02	150	951	5440
DD2-135135-0.04-H		0.04	150	951	5440
DD2-135135-0.01-M	(medium)	0.01	200	871	5790
DD2-135135-0.01-L	(low)	0.01	250	809	5690

Note. Here Δx_0, N, and L are the grid size of the inner region, grid number, and size of the computational domain, respectively (see text in Section 2.5). For all models, the DD2 EOS is employed, and the gravitational mass of each neutron star in a binary is 1.35 $M_\odot$.

2.5. Initial Condition and Grid Setting

The initial condition in this work is given by the same method as that in Fujibayashi et al. (2017): we first perform a three-dimensional, numerical-relativity simulation for the merger of equal-mass binary neutron stars with the total mass 2.7 $M_\odot$ (Sekiguchi et al. 2015) using DD2 EOS (Banik et al. 2014). For these choices of the total mass and EOS, the remnant formed after the merger is a long-lived MNS surrounded by a torus. At a few tens of ms after the formation of this system, the MNS and torus relax approximately to an axisymmetric configuration; hence, we employ such a system as the initial condition. The total baryon and Arnowitt–Deser–Misner (ADM) mass of the initial condition are ≈ 2.95 $M_\odot$ and 2.65 $M_\odot$, respectively. We note that ≈ 0.05 $M_\odot$ is carried by gravitational radiation during the inspiral and merger. The baryon mass of the torus of the initial condition is ≈ 0.2 $M_\odot$. Here we define the torus mass by

$$M_{\mathrm{b,torus}} = \int_{\rho < 10^{13} \mathrm{g\,cm}^{-3}} d^3 x \; \rho_*. \tag{16}$$

We note that the mass of the merger-remnant torus also depends on the total mass, mass ratio of the binary, and neutron star EOS. Therefore, the result in this work would be quantitatively different for different parameters and EOSs.

In addition to the dynamical variables employed in Fujibayashi et al. (2017), we need to prepare an initial condition for the spatial components of the viscous tensor τ_{ij}. For simplicity, we assume that the viscous tensor $\tau^0{}_{\alpha\beta}$ vanishes in the initial state. That is, as the initial condition for τ_{ij}, we set $\tau_{ij} = -\zeta h_{ij}$.

For evolving radiation-viscous hydrodynamics equations in cylindrical coordinates (x, z), we employ the same nonuniform grid as that in Fujibayashi et al. (2017), in which the grid structure is determined by the uniform grid spacing of the inner region, Δx_0; the range of the inner region, R_{star}; the increase rate of the grid spacing in the outer region, $1 + \delta$; and the grid number, N. For all the models in this paper, we set $R_{\mathrm{star}} = 30$ km and $\delta = 0.0075$. We list Δx_0 and N, together with the size of the computational domain, L, in Table 2. We performed simulations with three different viscosity parameters, $\alpha_{\mathrm{vis}} = 0.01$, 0.02, and 0.04, among which we refer to the model with $\alpha_{\mathrm{vis}} = 0.02$ as our fiducial model. Our choice of the viscosity parameter $\alpha_{\mathrm{vis}} = O(0.01)$ is justified, at least for the outer part of the MNS ($\rho \lesssim 10^{14}$ g cm^{-3}), by the recent high-resolution global MHD simulations for a binary neutron

star merger (Kiuchi et al. 2017). For a higher-density region, such as an inner region of the MNS, the value of the viscosity parameter is still uncertain, but for simplicity, we use the same value of the viscosity parameter for the entire region, supposing that a turbulence state would be achieved entirely in the MNS.[4]

To investigate the long-term evolution of the system, the simulations are performed for ~ 3 s for our fiducial and $\alpha_{\mathrm{vis}} = 0.04$ models, while the simulations of the other models are performed for a shorter time ($\lesssim 1$ s).

In addition to these models, to confirm that numerical results with different grid resolutions reasonably agree, we performed simulations for $\alpha_{\mathrm{vis}} = 0.01$ with two lower resolutions as $\Delta x_0 = 200$ m (M) and 250 m (L). The grid structure for these cases is also listed in Table 2. The result of this check is described in the Appendix.

2.6. Rates of Viscous Heating and Angular Momentum Transport in Our Formalism

From the component of Equation (2) along u^α, we obtain

$$-Q^\alpha_{(\mathrm{leak})} u_\alpha = -\rho u^\alpha \nabla_\alpha h + u^\alpha \nabla_\alpha P - u^\alpha \nabla^\beta (\rho h \nu \tau^0{}_{\alpha\beta})$$
$$= -\rho T u^\alpha \nabla_\alpha s + \rho h \nu \tau^0{}_{\alpha\beta} \nabla^\alpha u^\beta, \tag{17}$$

where we used the relation $\tau^0{}_{\alpha\beta} u^\alpha = 0$ and the first law of thermodynamics $dh = dP/\rho + T ds$, with T and s being the temperature and specific entropy. From the above relation, the viscous heating rate in the fluid rest frame in our formalism can be written approximately as

$$Q^{(+)}_{\mathrm{vis}} = \rho h \nu \tau^{0\,\alpha\beta} \nabla_\alpha u_\beta = \frac{1}{2} \rho h \nu \tau^{0\,\alpha\beta} \tau^0{}_{\alpha\beta}, \tag{18}$$

where we assumed that $\tau^0{}_{\alpha\beta}$ quickly approaches $\sigma_{\alpha\beta}$.

Using the y component of Equation (12), the angular momentum transport flux due to the viscous effect is described by

$$-\rho h \nu \bar{\tau}^{0\,i}{}_y = -\rho h \nu \gamma^{ik} \tau^0{}_{ky}. \tag{19}$$

From the surface integral of this, the local angular momentum transport rate is derived.

2.7. Timescales for Viscous Evolution

Before describing the numerical results, we estimate the timescales for the evolution of the MNS-torus system in the presence of viscosity. In this problem, the viscous effect plays two crucial roles.

In the first $\lesssim 20$ ms, the viscous effect plays an important role in the MNS. The MNS formed after the merger initially has a differentially rotating velocity profile. By the viscous effect, the angular momentum in a high angular velocity region is transported to a low angular velocity region; thus, the MNS approaches a rigidly rotating state. The timescale for the

---

[4] We note that for our choice of the parameters in Israel–Stewart formalism, ζ and $\nu = \alpha \rho h$, the causality is satisfied at least locally. Indeed, we do not find any pathological behavior of the fluid in our simulations, so we conclude that the causality is satisfied globally in our simulation.

angular momentum transport in the MNS is estimated by

$$\frac{R_{eq}{}^2}{\nu} \approx 10 \text{ ms} \left(\frac{\alpha_{vis}}{0.02}\right)^{-1} \left(\frac{c_s}{c/3}\right)^{-1}$$
$$\times \left(\frac{R_{eq}}{15 \text{ km}}\right)^2 \left(\frac{H_{tur}}{10 \text{ km}}\right)^{-1}, \quad (20)$$

where R_{eq} denotes the equatorial radius of the MNS. Thus, the differential rotation profile of the MNS is expected to be erased within $\sim 10 \, (\alpha_{vis}/0.02)^{-1}$ ms by the viscous effect.

For longer timescales, the viscous effect plays a primary role in determining the evolution of the torus surrounding the MNS. Assuming that the torus evolution could be described by a standard accretion disk theory (Shakura & Sunyaev 1973), the viscous accretion timescale is estimated by

$$t_{vis} \sim \alpha_{vis}{}^{-1} \left(\frac{R_{torus}{}^3}{GM_{MNS}}\right)^{1/2} \left(\frac{H}{R_{torus}}\right)^{-2}$$
$$\approx 0.55 \text{ s} \left(\frac{\alpha_{vis}}{0.01}\right)^{-1} \left(\frac{M_{MNS}}{2.5 \, M_\odot}\right)^{-1/2}$$
$$\times \left(\frac{R_{torus}}{50 \text{ km}}\right)^{3/2} \left(\frac{H/R_{torus}}{1/3}\right)^{-2}, \quad (21)$$

where M_{MNS} is the gravitational mass of the MNS, R_{torus} is the typical radius of the torus, and H/R_{torus} is the aspect ratio of the torus. Then, the mass accretion rate is estimated as

$$\dot{M}_{MNS} \sim \frac{M_{torus}}{t_{vis}}$$
$$\approx 0.36 \, M_\odot \text{ s}^{-1} \left(\frac{\alpha_{vis}}{0.01}\right) \left(\frac{M_{MNS}}{2.5 \, M_\odot}\right)^{1/2}$$
$$\times \left(\frac{R_{torus}}{50 \text{ km}}\right)^{-3/2} \left(\frac{H/R_{torus}}{1/3}\right)^2 \left(\frac{M_{torus}}{0.2 \, M_\odot}\right). \quad (22)$$

We note that in these estimates, we used the standard accretion disk in a stationary state as a model. In reality, the MNS-torus system is evolved by the viscous timescale (i.e., the values of R_{torus} and M_{torus} change with time); hence, we should check whether the stationary disk model is valid or not by performing the simulation of this system.

3. Result

3.1. Dynamics of the System

First, we briefly describe the evolution process of the system for the fiducial model DD2-135135-0.02-H.

In the early stage of the evolution, the angular momentum transport occurs in the MNS. Figure 1 shows the angular velocity profiles in the equatorial plane at different time slices for the fiducial model. This shows that initial differential rotation of the MNS within the radius of ~ 12 km disappears and the MNS settles into a rigid rotation state in ~ 10 ms, as estimated by Equation (20).

Then, a sound wave is formed in the vicinity of the MNS. This is due to the variation of the MNS density profile caused by the angular momentum redistribution.

The variation of the rotational kinetic energy in the redistribution of the rotational profile is approximately
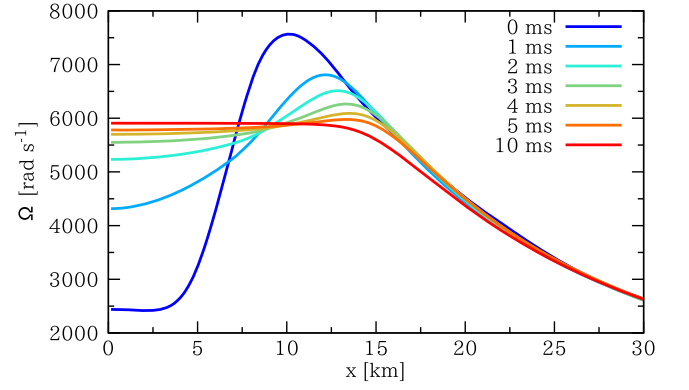

Figure 1. Angular velocity on the equatorial plane at $t = 0, 1, 2, 3, 4, 5,$ and 10 ms for the fiducial model DD2-135135-0.02-H ($\alpha_{vis} = 0.02$).

estimated by

$$\frac{1}{2}\Delta(v^2)M \sim \frac{1}{2}[\Delta(\Omega^2)R^2]M$$
$$\approx 2.3 \times 10^{52} \text{ erg} \left(\frac{\Delta(\Omega^2)}{9 \times 10^6 \text{ rad}^2 \text{ s}^{-2}}\right)$$
$$\times \left(\frac{R}{10 \text{ km}}\right)^2 \left(\frac{M}{2.5 M_\odot}\right), \quad (23)$$

where $\Delta(v^2)$ and $\Delta(\Omega^2)$ are the variations of the rotational velocity squared and angular velocity squared, and M is the mass suffered from this variation (approximately equal to M_{MNS}). This shows that the energy of $\sim 10^{52}$ erg could be redistributed in the inner region of the MNS in its viscous timescale, which is proportional to $\alpha_{vis}{}^{-1}$. This implies that the sound wave becomes stronger for the models with higher viscosity parameters.

During its outward propagation, the sound wave becomes a shock wave (see panel (1) of Figure 2). It sweeps the material surrounding the torus and then induces mass ejection of the material for the first ~ 50 ms (see panels (1) and (2) of Figure 2). We refer to this mass ejection as "early viscosity-driven mass ejection."

The material swept up by the shock wave for small radii ($r \lesssim 500$ km) is still gravitationally bound while it continues to expand for ~ 0.1 s, as shown in panel (3) of Figure 2. After ~ 0.1 s, the material begins to turn over and fall again (see panel (4) of Figure 2). We note that for the model with $\alpha_{vis} = 0.04$, this turnover occurs only weakly and more mass is ejected from the system (see the discussion of Section 3.4.2).

After the early viscosity-driven mass ejection, the neutrino- and viscosity-driven mass ejection is developed in the polar region. It is difficult to separate the contributions of the heating due to the neutrino irradiation and viscosity, but for $t \gtrsim 0.2$ s, the viscous heating becomes important rather than the neutrino heating. This is because the neutrino pair-annihilation heating, which is the primary neutrino heating source, plays a minor role due to the decrease of the neutrino luminosity in this phase for the inviscid model (Fujibayashi et al. 2017).

The material in the torus moves in various directions for the first tens of ms (see panel (1) of Figure 2), but the flow structure gradually relaxes to a laminal state due to the viscosity-driven redistribution (see panels (3) and (4) of Figure 2). After the relaxation, the MNS-torus system evolves in a quasi-stationary manner. The torus material around the equatorial plane expands
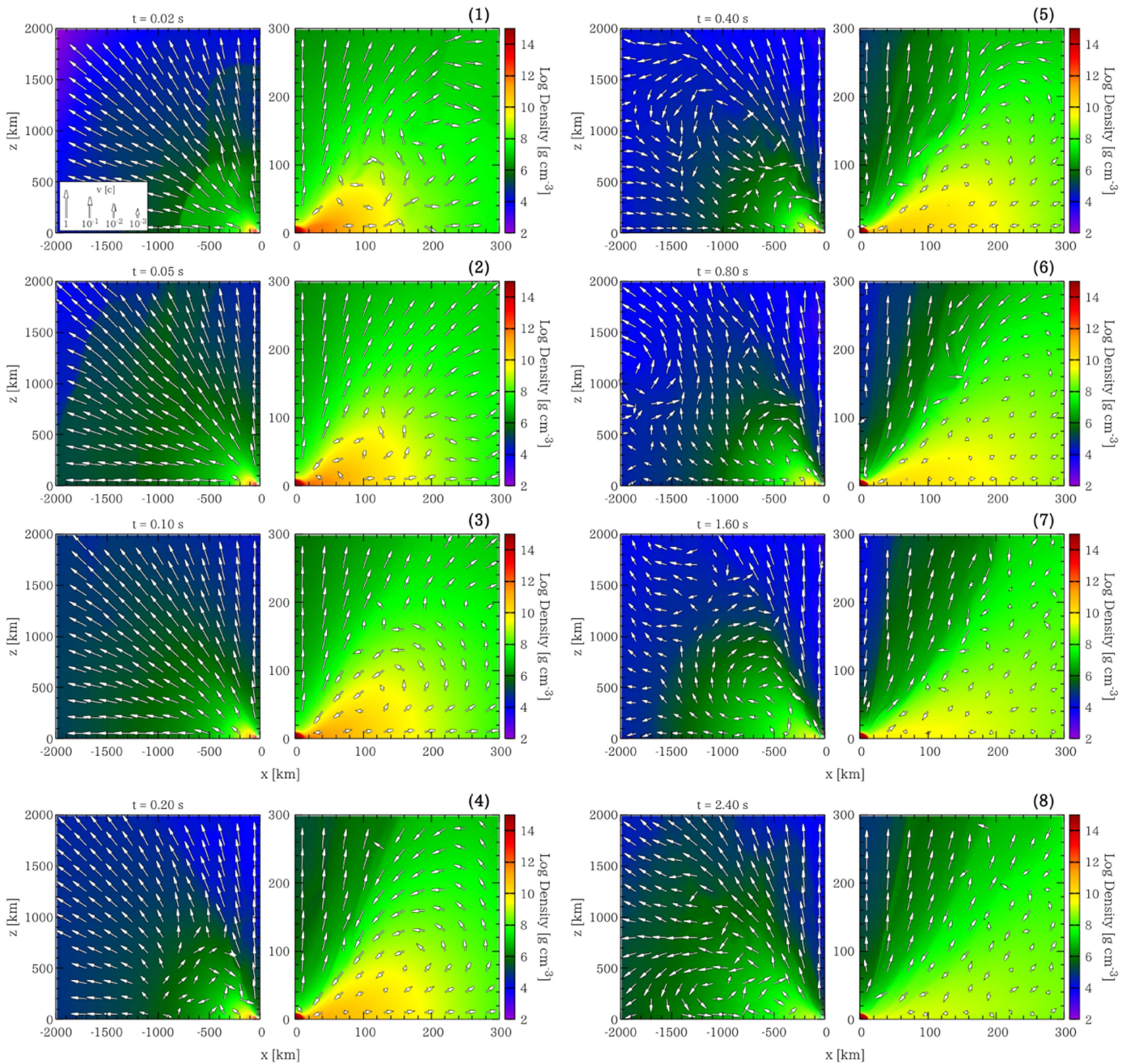
Figure 2. Snapshots of the density and poloidal velocity field for the fiducial model DD2-135135-0.02-H at $t = 0.02, 0.04, 0.1, 0.2, 0.4, 0.8, 1.6$, and 2.4 s. The length of the velocity vector corresponds to the logarithm of the poloidal velocity. The scale is shown in panel (1). For each panel, the left and right subpanels show the wide region ($r \lesssim 2000$ km) and narrow region ($r \lesssim 300$ km), respectively.

outward, while the torus material near the torus surface accretes onto the central MNS (see also Figure 5 in Section 3.2). Figure 3 shows the density profiles on the equatorial plane at different time slices. As found in this figure, the torus gradually expands with time; hence, the torus density decreases. This behavior of the torus is determined by the viscous angular momentum transport (see Section 3.2 for details).

The top and middle panels of Figure 4 show the time evolution of the baryon mass and the angular momentum of the torus defined by

$$J_{\rm torus} = \int_{\rho < 10^{13}{\rm g\ cm^{-3}}} d^3x\ \rho_* h u_y x. \tag{24}$$

For all of the models, they decrease with time due to mass accretion onto the central MNS and outflow.[5]

In the phase of the early viscosity-driven mass ejection, in which the density profiles of the MNS and torus vary in a short timescale, the decrease timescale is slightly shorter than that estimated by Equation (21). However, after the torus relaxes to a quasi-stationary state, the timescale agrees approximately with that by Equation (21).

---

[5] Here $M_{\rm b,torus}$ and $J_{\rm torus}$ slowly decrease even in the inviscid model. This inflow is due to the cooling of the torus by the neutrino emission; the loss of the pressure support causes the torus accretion.
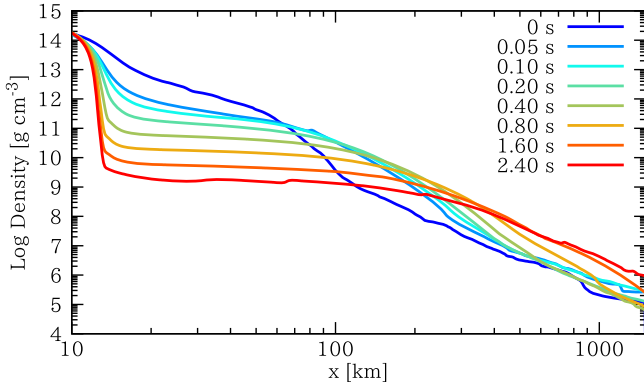
Figure 3. Density profiles on the equatorial plane for the fiducial model at 0, 0.05, 0.1, 0.2, 0.4, 0.8, 1.6, and 2.4 s.
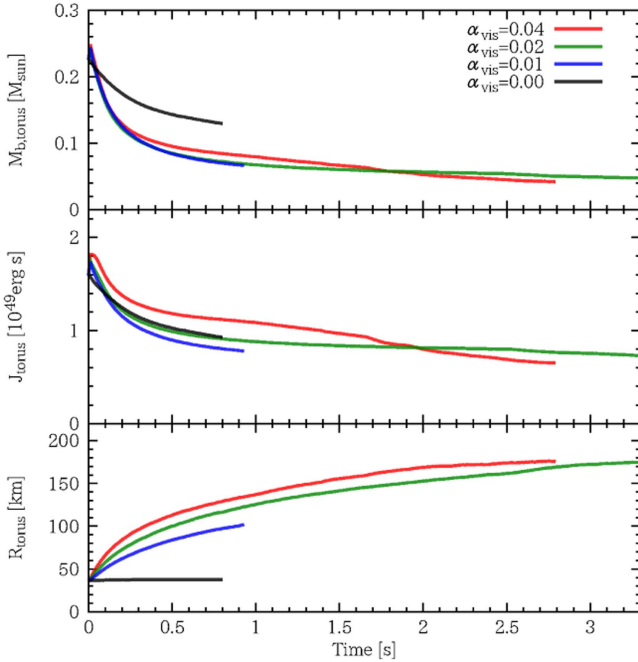

Figure 4. Time evolution of the baryon mass (top), angular momentum (middle), and typical radius (bottom) of the torus. The baryon mass, angular momentum, and typical radius of the torus are defined by Equations (16), (24), and (25), respectively. For all panels, the different colors of the curves indicate the results for models DD2-135135-0.00-H, DD2-135135-0.01-H, DD2-135135-0.02-H, and DD2-135135-0.04-H.

The decrease rates of $M_{\rm b,torus}$ and $J_{\rm torus}$ approach zero for $t \gtrsim 1$ s. This implies that the accretion onto the MNS becomes inefficient. This point will be revisited in Section 3.3.

Because the angular momentum profile of the torus is approximately described by the Keplerian profile around the MNS, we define a typical torus radius by

$$R_{\rm torus} \equiv \frac{J_{\rm torus}^2}{GM_{\rm b,torus}^2} \frac{1}{M_{\rm MNS}}$$

$$\approx 70 \text{ km} \left(\frac{J_{\rm torus}}{10^{49} \text{ erg s}}\right)^2 \left(\frac{M_{\rm b,torus}}{0.1\ M_\odot}\right)^{-2} \left(\frac{M_{\rm MNS}}{2.6\ M_\odot}\right)^{-1}. \quad (25)$$

Here we assumed that $J_{\rm torus}$ would be approximately given by $M_{\rm b,torus}\sqrt{GM_{\rm MNS}R_{\rm torus}}$. The bottom panel of Figure 4 shows the radii for all the models. Here we used $M_{\rm MNS} = 2.6\ M_\odot$ for all of the models, which is approximately equal to the ADM mass

of the system. The typical radius is 30–40 km at the beginning of the simulation. For the viscous models, it increases with time, while the radius is approximately constant in time for the inviscid model. This shows that, by viscous angular momentum transport, the torus expands along the equatorial direction. This effect eventually induces viscosity-driven mass ejection from the torus. We will describe this process in Section 3.4.

3.2. Structure of the Quasi-stationary Flow for 0.1 s $\lesssim t \lesssim$ 2 s

When the central remnant composed of a rigidly rotating MNS and torus relaxes to a quasi-stationary state, the flow structure also reaches a quasi-stationary state approximately. This state is preserved until the matter temperature of the torus decreases sufficiently. The top right panel of Figure 5 shows the radial mass flux in the meridian plane at $t = 0.2$ s for the fiducial model. Broadly speaking, the structure of the flow is divided into three parts: the outflow near the polar region (Region I; red), the expanding flow along the equatorial plane (Region II; red), and inflow between the two regions (Region III; blue).

The top left panel of Figure 5 displays the profile of the source of the angular momentum transport due to the viscosity (i.e., $x^{-2}\partial_j(x^2\rho h\nu\bar\tau^{0j}{}_y)$). This panel also shows the direction of the angular momentum flux due to the viscosity (i.e., $-\rho h\nu(\bar\tau^x{}_y, \bar\tau^z{}_y)$). This clearly illustrates that the angular momentum is transported from Region III to Region II. Therefore, the expanding part in Region II is driven by the angular momentum transport from the inflow in Region III.

The top left panel of Figure 6 shows the vertically and azimuthally integrated heating rate (solid red curve)

$$\mathcal{H} = 2 \int_0^L dz\ 2\pi x\ (Q_{\rm vis}^{(+)} + Q_\nu^{(+)}) \quad (26)$$

and cooling rate (solid blue curve)

$$\mathcal{C} = 2 \int_0^L dz\ 2\pi x\ Q_{\rm (leak)}^{(-)}. \quad (27)$$

Here $Q_\nu^{(+)}$ is the sum of the matter-heating source terms due to the neutrino absorption and pair-annihilation processes (see Fujibayashi et al. 2017 for the description of the individual heating rates) and $Q_{\rm (leak)}^{(-)}$ is the sum of the leakage source terms for all flavors of neutrinos. This figure shows that the viscous heating rate balances approximately with the net neutrino cooling rate.

In the same panel, the heating and cooling rates in the outgoing and ingoing regions,

$$\mathcal{H}_{\left\{{< \atop >}\right\}} = 2 \int_{0,\left\{{v^x<0 \atop v^x>0}\right\}}^L dz\ 2\pi x\ (Q_{\rm vis}^{(+)} + Q_\nu^{(+)}), \quad (28)$$

$$\mathcal{C}_{\left\{{< \atop >}\right\}} = 2 \int_{0,\left\{{v^x<0 \atop v^x>0}\right\}}^L dz\ 2\pi x\ Q_{\rm (leak)}^{(-)}, \quad (29)$$

are plotted in the dashed and dotted curves, respectively. These clearly show that the balances between the viscous heating and the net neutrino cooling are approximately achieved both in Region II (expanding region) and Region III (inflowing region). This indicates that the neutrino-dominated accretion flow (NDAF) is achieved in Region III.

The middle left panel of Figure 6 shows the mass inflow and outflow rates ($\dot M_{\rm in}$ and $\dot M_{\rm out}$) along the equatorial plane, together
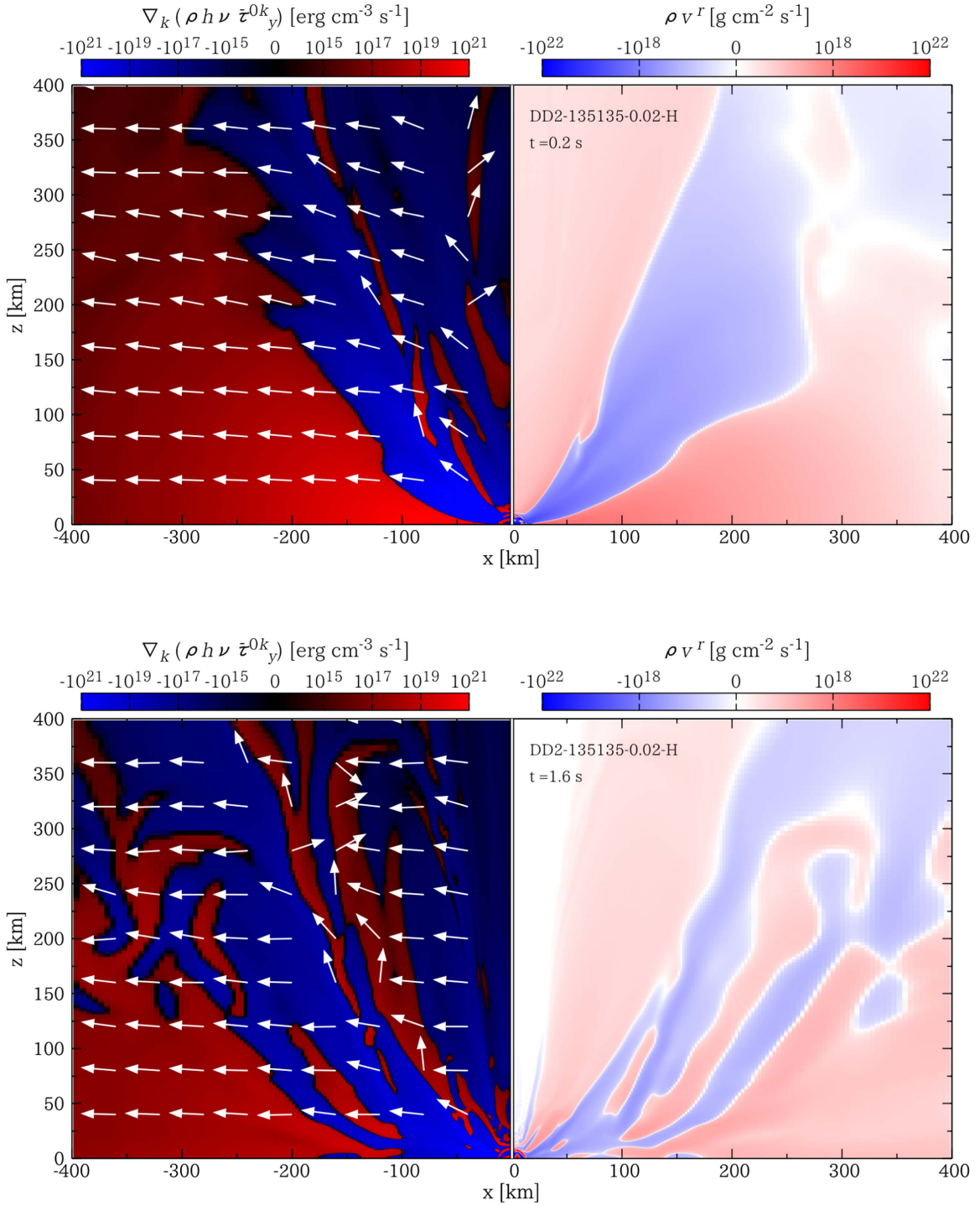
Figure 5. Snapshot of the viscous angular momentum flux (left panels) and radial mass flux (right panels) for the fiducial model at $t = 0.2$ s (top) and 1.6 s (bottom). The vector field represents only the direction of the poloidal angular momentum flux $-\rho h \nu (\bar{\tau}^{0x}_{\ y}, \bar{\tau}^{0z}_{\ y})$.

with the net rates $(\dot{M})$, defined, respectively, by

$$\dot{M}_{\rm in} = -2 \int_{0,v^x<0}^{L} dz\ 2\pi x \rho_* v^x, \qquad (30)$$

$$\dot{M}_{\rm out} = 2 \int_{0,v^x>0}^{L} dz\ 2\pi x \rho_* v^x, \qquad (31)$$

and

$$\dot{M} = \dot{M}_{\rm in} - \dot{M}_{\rm out}. \qquad (32)$$

In the same panel, we plot the mass accretion rate in the "standard" disk picture, i.e., a stationary thin accretion disk,

$$\dot{M}_{\rm sd} \approx 3\pi\nu\Sigma. \qquad (33)$$

Here we neglected the terms from the inner boundary condition and defined the column density of the torus by $\Sigma = 2\rho c_s/\Omega|_{z=0}$, which is evaluated using the values on the equatorial plane. The net mass accretion rate $\dot{M}$ agrees
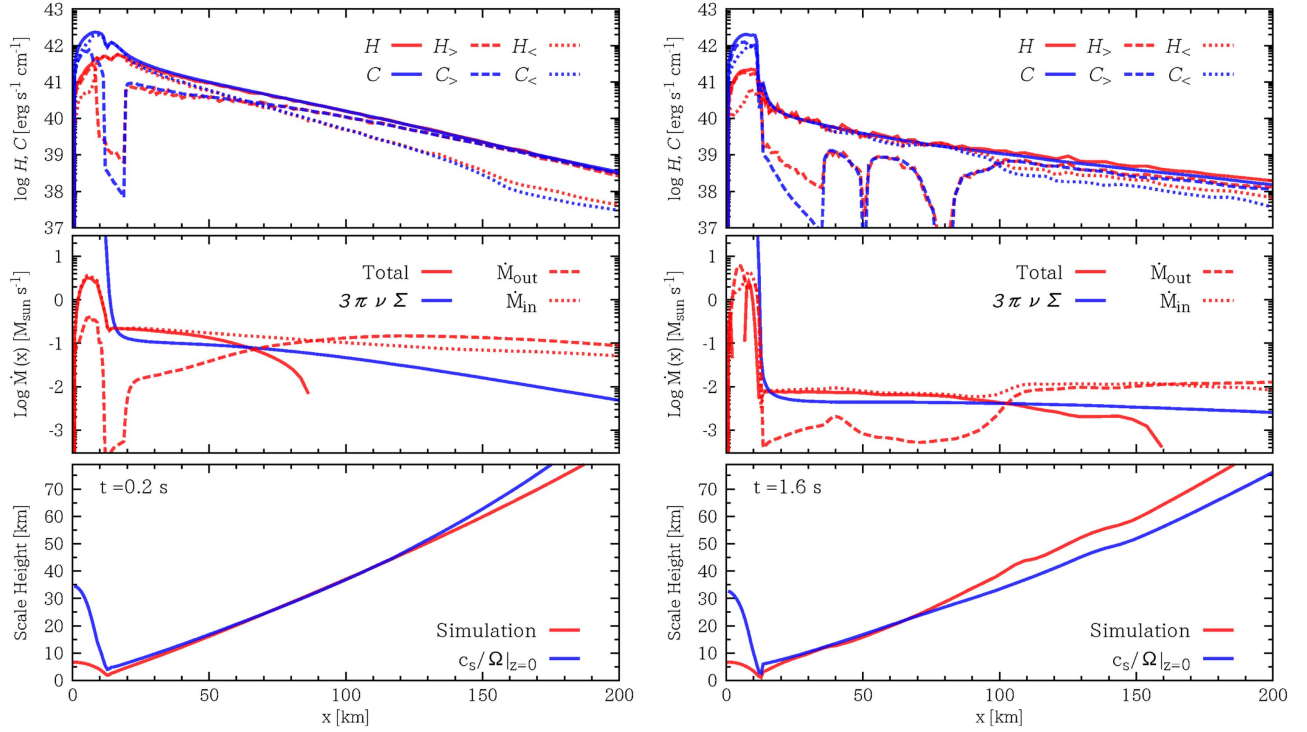
Figure 6. Flow structure for the fiducial model at $t = 0.2$ s (left panels) and 1.6 s (right panels). Top: vertically integrated heating and cooling rates. In addition to the total rate (i.e., Equations (26) and (27)) shown by the solid curves, the heating and cooling rates integrated over only for $v^x < 0$ or $v^x > 0$ region (i.e., Equations (28) and (29)) are shown by the dotted and dashed curves, respectively. Middle: mass accretion and outflow rates. The solid red curve indicates the net accretion rate defined by Equation (32), and the dotted and dashed curves indicate the mass inflow and outflow rates defined by Equations (30) and (31), respectively. The solid blue curve indicates the mass accretion rate defined by Equation (33). Bottom: scale height of the torus. The red curve indicates the scale height defined by Equation (34), and the blue curve indicates the scale height obtained by assuming the hydrostatic structure in the vertical direction, i.e., $c_s / \Omega|_{z=0}$.

approximately with the accretion rate in the standard disk picture $\dot{M}_{sd}$ for the innermost region of the torus $x \lesssim 50$ km.

In the bottom left panel of Figure 6, we compare the scale height of the torus assuming the vertically hydrostatic structure $H_{sd} = c_s / \Omega|_{z=0}$ and the scale height calculated from the simulation data H_{num} to check the validity of the approximation of the flow as the standard disk. Here H_{num} is defined as

$$\rho(z = H_{num}) = \rho(z = 0)/e, \qquad (34)$$

where e is the base of natural logarithms. In the innermost region ($x \lesssim 100$ km) of the torus, the two scale heights agree well.

The flow structure, heating and cooling rates, mass accretion rate, and scale height at the late time $t = 1.6$ s are shown in the bottom panels of Figure 5 and the right panels of Figure 6, respectively. We find in Figure 5 that the flow structure at $t = 1.6$ s is qualitatively the same as that at $t = 0.2$ s, while the mass flux becomes smaller than that in the early phase (see the middle panel of Figure 6). At $t = 1.6$ s, the region for which the net mass accretion rate agrees with the standard picture accretion rate is wider than that at $t = 0.2$ s.

To conclude, the global structure of the flow can be described approximately by the standard NDAF for a long timescale 0.1 s $\lesssim t \lesssim 2$ s.

3.3. Mass Accretion onto the MNS

The top panel of Figure 7 shows the accretion rate of the torus material onto the MNS, which is defined by the radial
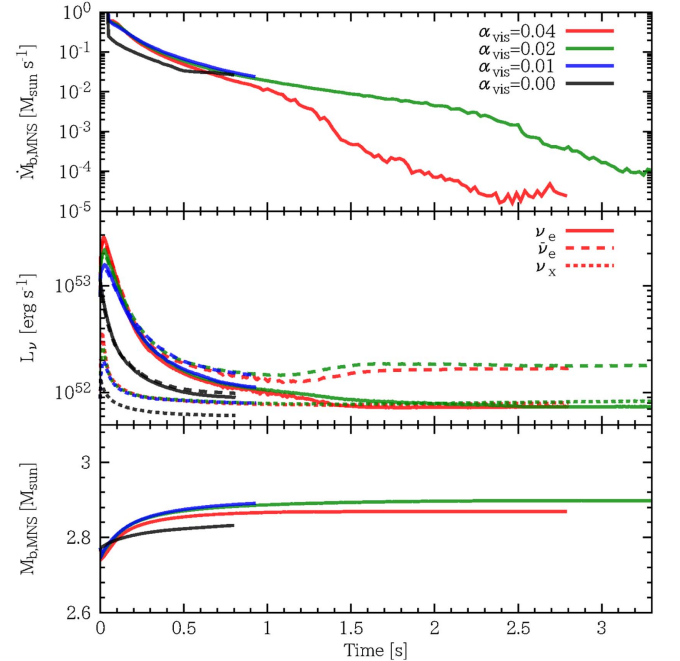

Figure 7. Time evolution of the mass accretion rate (top), neutrino emission rate (middle), and baryon mass of the MNS (bottom). The baryon mass of the MNS is defined by Equation (35). In the middle panel, the emission rates of electron neutrinos, electron antineutrinos, and other neutrino species are shown by the solid, dashed, and dotted curves, respectively. For all panels, the different colors of the curves indicate the results for models DD2-135135-0.00-H, DD2-135135-0.01-H, DD2-135135-0.02-H, and DD2-135135-0.04-H.
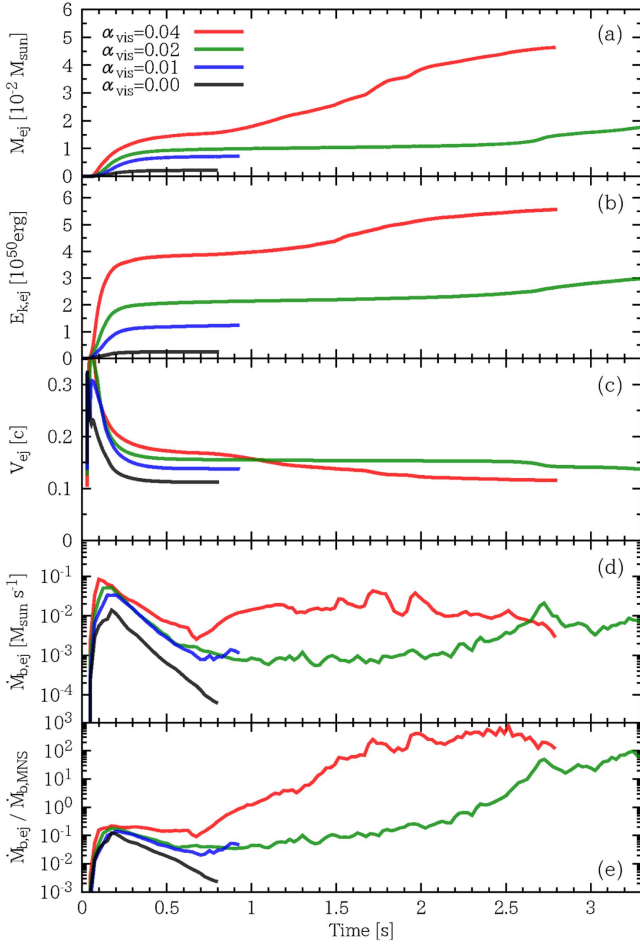
Figure 8. Time evolution of the baryon mass (panel (a)), kinetic energy (panel (b)), and average velocity (panel (c)) of the ejecta, mass ejection rate (panel (d)), and ratio of $\dot{M}_{\rm b,ej}$ to $\dot{M}_{\rm b,MNS}$ (panel (e)). For all panels, the different colors of the curves indicate the results for models DD2-135135-0.00-H, DD2-135135-0.01-H, DD2-135135-0.02-H, and DD2-135135-0.04-H.

mass inflow rate (i.e., Equation (32)) at $x = 20$ km. The mass accretion rate is $\sim 0.5\ M_\odot\ {\rm s}^{-1}$ at ~ 0.1 s, which is consistent with the estimation in Equation (22). The mass accretion rate monotonically decreases, and it becomes $\sim 0.004\ M_\odot\ {\rm s}^{-1}$ at $t = 2$ s for the fiducial model. This decrease stems partly from the decrease of the torus mass, but the major reason is the radial expansion of the torus due to the outward angular momentum transport, as described in the previous subsection. Unlike the estimation of Equation (22), the mass accretion rate for $t \lesssim 1$ s depends only weakly on $\alpha_{\rm vis}$ (compare the results for $\alpha_{\rm vis} = 0.01$, 0.02, and 0.04). This is because the typical radius of the torus becomes large more rapidly for the model with higher viscosity parameters (see the bottom panel of Figure 4). The mass accretion rate for $t \gtrsim 1$ s depends on $\alpha_{\rm vis}$; the rate for the model with $\alpha_{\rm vis} = 0.04$ decreases more rapidly than that for the fiducial model. This is because the neutrino cooling in the torus becomes inefficient at the earlier time; hence, the torus material starts being ejected rather than accreted onto the MNS (see Section 3.4 for details).

The middle panel of Figure 7 shows the time evolution of the neutrino emission rates. Because of the presence of the viscous heating, the neutrino emission rate for $\alpha_{\rm vis} \neq 0$ is higher than that of the inviscid model. For the viscous models, the high emission rate of $\sim 10^{53}\ {\rm erg\ s}^{-1}$ is sustained for ~ 0.1 s.

However, for the late time $t \gtrsim 1$ s, the emission rate decreases to $\sim 10^{52}\ {\rm erg\ s}^{-1}$ as the accretion rate, $\dot{M}_{\rm b,MNS}$, decreases. Since the mass accretion rate depends weakly on $\alpha_{\rm vis}$ for $t \lesssim 1$ s, the neutrino emission rate also depends weakly on the viscosity parameter.

The bottom panel of Figure 7 shows the baryon mass of the MNS, defined by

$$M_{\rm b,MNS} = \int_{x < 20\ {\rm km}} d^3x\ \rho_*. \qquad (35)$$

As found from the top panel of Figure 7, the MNS mass increases with time, but eventually, it is saturated because the mass accretion from the torus decreases significantly. The final relaxed value, $\approx 2.9\ M_\odot$, depends only weakly on $\alpha_{\rm vis}$.

For the DD2 EOS, the MNS with $M_{\rm b,MNS} = 2.9\ M_\odot$ does not collapse to a black hole, at least in a few seconds after the onset of the merger, because the maximum gravitational mass for cold spherical neutron stars for this EOS is quite high, 2.42 $M_\odot$. However, for softer EOSs, in which the maximum gravitational mass is smaller, say 2.1 $M_\odot$, the remnant MNS of the baryon mass of $\sim 2.9\ M_\odot$ may collapse to a black hole due to the mass accretion.

3.4. Mass Ejection

3.4.1. Early Viscosity-driven Mass Ejection

Panel (a) of Figure 8 shows the evolution of the baryon mass of the ejecta, which is calculated by integrating the flux of the unbound material at an outer surface as

$$
\begin{aligned}
M_{\rm b,ej}(t) &= \int_0^t dt'\ 2 \int dS_k\, \rho_* v^k \Theta(|hu_t| - 1) \\
&= \int_0^t dt'\ 2 \int_0^{L_{\rm bnd}} dx\ 2\pi x \rho_* v^z \Theta(|hu_t| - 1) \\
&\quad + \int_0^t dt'\ 2 \int_0^{L_{\rm bnd}} dz\ 2\pi x \rho_* v^x \Theta(|hu_t| - 1), \quad (36)
\end{aligned}
$$

where dS_k is the two-dimensional area element on a cylinder of both radius and height $L_{\rm bnd}$. Here we set $L_{\rm bnd} = 4000$ km and suppose that fluid elements with $|hu_t| > 1$ are gravitationally unbound.[6]

This figure shows that the mass ejection rate in the early phase $t \lesssim 0.2$ s is rather high, 0.03–0.1 $M_\odot\ {\rm s}^{-1}$. This is achieved by the early viscosity-driven ejecta (see Section 3.1).

We also calculate the evolution of the total ejecta energy by

$$E_{\rm tot,ej}(t) = \int_0^t dt' \int dS_k\, \rho_* \hat{e}_0 v^k \Theta(|hu_t| - 1). \qquad (37)$$

Using $E_{\rm tot,ej}$ and $M_{\rm b,ej}$, the kinetic energy of the ejecta is defined by

$$E_{\rm kin,ej} = E_{\rm tot,ej} - M_{\rm b,ej}, \qquad (38)$$

which is shown in panel (b) of Figure 8. Here we assumed that the internal energy of the ejecta would be totally transformed into the kinetic energy during the subsequent expansion. Unlike

---

[6] We note that this criterion may overestimate the amount of the ejecta, since some amount of the thermal energy is radiated by neutrinos before the energy is transformed into the kinetic energy. However, the temperature of the material at $L_{\rm bnd} = 4000$ km is lower than 0.1 MeV, for which the neutrino cooling timescale is much longer than the expansion timescale, and thus the estimation of the ejecta mass works reasonably.

the mass accretion rate and the neutrino emission rate shown in Section 3.3, the mass and kinetic energy of the ejecta increase monotonically with $\alpha_{\rm vis}$ for $t \lesssim 0.2$ s.

Panel (c) shows the evolution of the average velocity of the ejecta, which is defined by $V_{\rm ej} = \sqrt{2E_{\rm k,ej}/M_{\rm b,ej}}$. For the early viscosity-driven ejecta, which is ejected for $t \lesssim 0.2$ s, the average velocity is in the range 0.15–0.2 c and monotonically increases with $\alpha_{\rm vis}$ as the mass and kinetic energy of the ejecta. This is because the shock driven by the early viscous effect on the MNS is stronger for the higher viscosity parameter model.

In our simulations, we suppose that the viscosity suddenly arises after the merger remnant settles to a quasi-stationary state. We should note that the variation of the quasi-equilibrium configuration occurs only if the viscous effect is enhanced after the dynamical phase of the merger ends, e.g., by MHD turbulence induced by the significantly amplified magnetic fields at the onset of the merger (Kiuchi et al. 2014, 2015b, 2017). If the viscosity in the MNS arises slowly enough, the variation of the quasi-stationary states occurs smoothly, so that the density wave would not appear strongly at the MNS surface and the mass ejection due to the shock would not occur significantly.

3.4.2. Late-time Viscosity-driven Mass Ejection

The mass ejection for $t \gtrsim 0.2$ s is driven primarily by the viscous effects in the torus. The ejecta is launched mainly toward the polar region for the relatively early time with $t \lesssim 1$ s, as found in panels (4)–(6) of Figure 2. However, the major mass ejection mechanism is subsequently changed as discussed below. In the following, we focus only on the models for $\alpha_{\rm vis} = 0.02$ and 0.04 because long-term simulations are performed only for these models.

Figure 9 shows the evolution of the mass, kinetic energy, and average velocity of the ejecta that becomes unbound after $t = 0.5$ s for the components toward the polar direction of $0° \leqslant \theta \leqslant 30°$ and the other (equatorial) direction of $30° < \theta \leqslant 90°$, respectively. From this figure, it is found that the material ejected toward the polar direction is smaller than or approximately as large as that ejected toward the equatorial direction. On the other hand, the polar ejecta has larger kinetic energy than the equatorial ejecta because the average velocity of the polar ejecta is larger ($\sim 0.15\,c$) than that of the equatorial ejecta ($\sim 0.05\,c$). This clearly shows that there are two components for the ejecta in the late time. We note that the two components are distinct because they are launched from completely different regions in the system. The polar ejecta is launched from the vicinity of the MNS, while the equatorial ejecta is launched from the outer region of the torus.

As found in the top panel of Figure 9, for $\alpha_{\rm vis} = 0.04$, the mass ejection in this late phase (for $t \gtrsim 0.5$ s) is primarily toward the equatorial direction, while for the fiducial model ($\alpha_{\rm vis} = 0.02$), the equatorial mass ejection is as weak as the polar one up to $t \sim 2.7$ s. For $\alpha_{\rm vis} = 0.04$, the early viscosity-driven mass ejection continues for a later time than that for the fiducial ($\alpha_{\rm vis} = 0.02$) model because the shock driven by the early viscous effect on the MNS is stronger for the larger viscosity parameter models. This is the reason for the larger mass ejection rate toward the equatorial direction for $\alpha_{\rm vis} = 0.04$ than that for the fiducial model for $t \lesssim 0.8$ s. On the other hand, the reason for the rapid increase of the mass ejection rate for $t \gtrsim 0.8$ s is the viscous effect on the torus. The torus expands due to the viscous angular momentum transport;
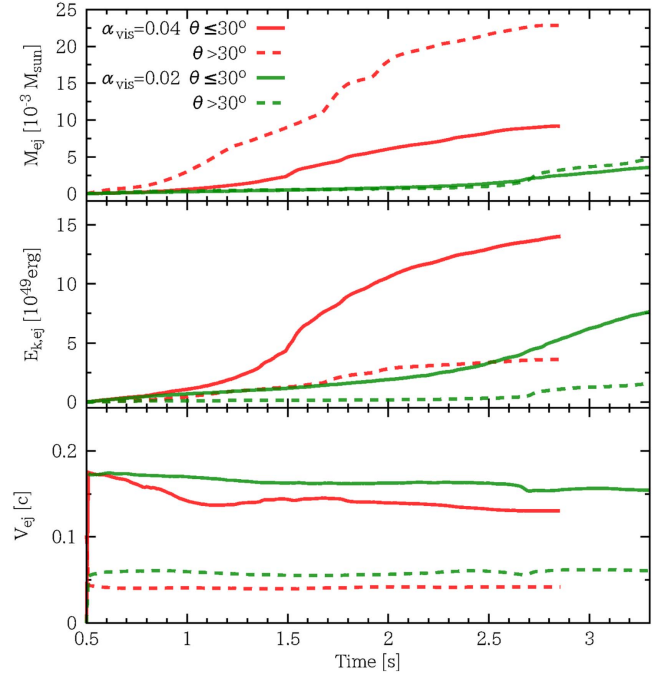

Figure 9. Same as panels (a)–(c) of Figure 8 but for the material ejected toward the polar angle $0° \leqslant \theta \leqslant 30°$ (solid curves) and $30° < \theta \leqslant 90°$ (dotted curves) by the late-time viscosity-driven mass ejection for $t \geqslant 0.5$ s for the models DD2-135135-0.02-H (red curves) and DD2-135135-0.04-H (green curves), respectively.

hence, its density and temperature decrease. As a result, the neutrino cooling becomes inefficient in the outer region of the torus. Then, the materials in the outer region can be ejected toward the equatorial region by the viscous heating and angular momentum transport without suffering from the neutrino cooling.

This late-time viscosity-driven mass ejection from the torus is first suggested in Fernández & Metzger (2013) and Metzger & Fernández (2014) and is also found in Just et al. (2015). The velocity of the ejecta in our work, $\sim 0.05\,c$, as well as the mass ejection mechanism, is totally consistent with their results. We confirm their results in a more realistic setup with an initial condition derived from three-dimensional simulation by a fully general relativistic simulation that self-consistently solves the evolution of both the MNS and the torus surrounding the MNS.

After the neutrino cooling becomes subdominant in the torus, the torus expands in the viscous timescale defined by Equation (21); hence, this late-time mass ejection rate can be estimated by dividing the torus mass by the viscous timescale as

$$\dot{M} \sim \frac{M_{\rm b,torus}}{t_{\rm vis}}$$

$$\sim 0.012\, M_\odot\, {\rm s}^{-1} \left(\frac{\alpha_{\rm vis}}{0.04}\right)\left(\frac{H_{\rm tur}}{10\ {\rm km}}\right)^2$$

$$\times \left(\frac{M_{\rm b,torus}}{0.05\, M_\odot}\right)\left(\frac{R_{\rm torus}}{100\ {\rm km}}\right)^{-7/2}\left(\frac{M_{\rm MNS}}{2.6\, M_\odot}\right)^{1/2}, \qquad (39)$$

where we used the torus mass for $t \gtrsim 1$ s (see the top panel of Figure 4). This mass ejection rate agrees reasonably well with our results (see panel (d) of Figure 8).
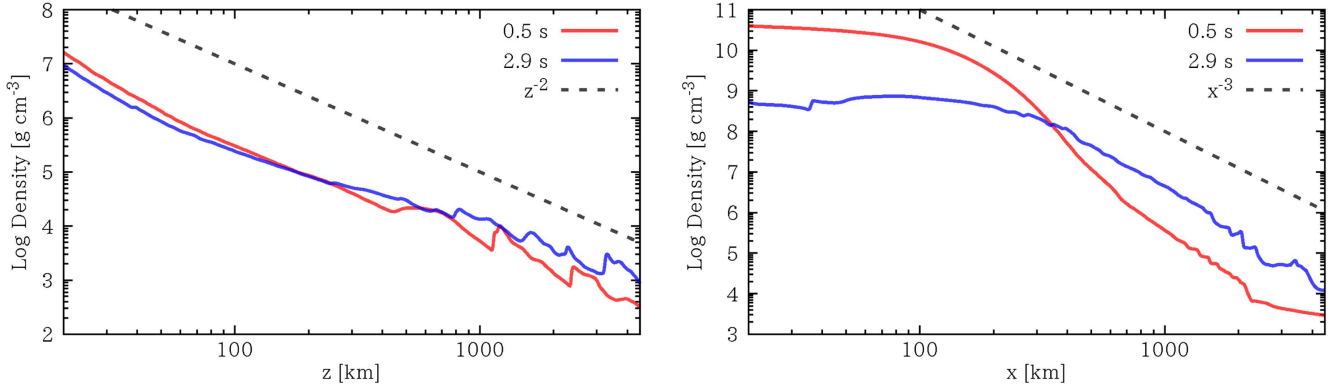
Figure 10. Density profiles on the rotational axis (left) and equatorial plane (right) at 0.5 s (red curves) and 2.9 s (blue curves) for the fiducial model.

For the fiducial model, this late-time equatorial viscosity-driven mass ejection also sets in at $t \sim 2.7$ s. As found in the last panel of Figure 2, the velocity in the dense region ($\rho \sim 10^7 \, \mathrm{g \, cm^{-3}}$) turns outward. In addition, the top panel of Figure 9 indicates that the equatorial mass ejection rate increases for $t \gtrsim 2.7$ s. The time delay for the onset of the late-time viscosity-driven mass ejection toward the equatorial plane for the smaller value of α_{vis} is simply due to the less viscous power.

The mass ejection efficiency, defined by $\dot{M}_{\mathrm{b,ej}}/\dot{M}_{\mathrm{b,MNS}}$, is shown in panel (e) of Figure 8. We find that this ratio becomes larger than unity for $t \gtrsim 1$ and $t \gtrsim 2.3$ s for $\alpha_{\mathrm{vis}} = 0.04$ and 0.02, respectively, and it eventually exceeds 10 because the mass accretion onto the MNS approaches zero. Therefore, a large fraction of the torus material, which is $\sim 0.05 \, M_\odot$ at $t \gtrsim 1$ s (see the top panel of Figure 4), is likely to be ejected from the system eventually. This speculation is supported by the result for the model with $\alpha_{\mathrm{vis}} = 0.04$, for which the mass of the late-time equatorial viscosity-driven ejecta is already $\sim 0.05 \, M_\odot$ at $t \sim 2.7$ s.

For the $\alpha = 0.02$ model, a large fraction of the material that would eventually be ejected is still in the region $0 \leqslant x < L_{\mathrm{bnd}}$ and $0 \leqslant z < L_{\mathrm{bnd}}$; hence, they are still not considered an ejecta at the end of the simulations. The main neutrino emitter is the MNS for $t \gtrsim 0.5$ s, and the neutrino emission rate is $\sim 10^{52} \, \mathrm{erg \, s^{-1}}$. For this emission rate, the timescale for the neutrino absorption

$$\frac{4\pi r^2 \langle \omega \rangle}{L_\nu} \frac{1}{G_{\mathrm{F}}^2 \langle \omega \rangle^2}$$

$$\sim 0.4 \, \mathrm{s} \left(\frac{\langle \omega \rangle}{10 \, \mathrm{MeV}} \right)^{-1} \left(\frac{L_\nu}{10^{52} \, \mathrm{erg \, s^{-1}}} \right)^{-1} \left(\frac{r}{100 \, \mathrm{km}} \right)^2 \quad (40)$$

is much longer than the time for the expansion timescale

$$r/v \sim 7 \times 10^{-3} \, \mathrm{s} \left(\frac{r}{100 \, \mathrm{km}} \right) \left(\frac{v}{0.05 \, c} \right)^{-1}. \quad (41)$$

Thus, the electron fraction of the material in the outer part of the torus, which is in the range 0.3–0.4, is frozen out; hence, the electron fraction of the material that would eventually be ejected is also in the range 0.3–0.4.

Figure 10 shows the density profiles on the rotational axis (left panel) and equatorial plane (right panel) for the fiducial model. We find that the density decreases approximately in proportion to z^{-2} along the rotational axis. This behavior does not depend strongly on the time, since the polar mass ejection

develops from the early phase of the evolution of the system. On the other hand, along the equatorial plane, the density for the large radius ($x \gtrsim 500$ km) decreases in proportion approximately to x^{-3} after the equatorial viscosity-driven mass ejection sets in (see the blue curve in the right panel). This radius dependence does not change significantly in time for the late phase ($t \gtrsim 2.7$ s); hence, we expect that the density structure of the equatorial ejecta is also proportional approximately to x^{-3}. This radius dependence of the equatorial ejecta is similar to that of the dynamical ejecta with a velocity $\lesssim 0.4 \, c$ (Nagakura et al. 2014).

To summarize this subsection, we find two mass ejection mechanisms for the system composed of the long-lived MNS and torus. One is the early viscosity-driven mass ejection, in which the differential rotation of the MNS is the engine, and the other is the late-time viscosity-driven mass ejection from the torus, in which the differential rotation of the torus is the engine. Specifically, there are two different components for the late-time viscosity-driven ejecta from the torus, one of which is the viscosity-driven ejecta toward the polar direction in assistance with the neutrino irradiation, and the other is launched primarily toward the equatorial direction in the later phase for which the neutrino cooling becomes inefficient because the temperature of the torus decreases sufficiently (see Table 3 for a summary).

4. Discussion

4.1. Overall Mass Ejection Processes of the Merger and Post-merger of Binary Neutron Stars

Here we discuss the properties of the ejecta for individual mass ejection processes based on the results of our numerical-relativity simulations.

We summarize possible mass ejection processes in the merger and post-merger phases in Figure 11. First, during the merger, the dynamical mass ejection occurs (e.g., Hotokezaka et al. 2013b; Sekiguchi et al. 2015, 2016). This mass ejection proceeds for ~ 10 ms primarily toward the equatorial direction. The ejecta mass depends on the stiffness of the neutron star EOS, total mass, and mass ratio of the binary, and it is in the range 0.001–0.02 $M_\odot$. For the DD2 EOS, which is used in this work, it is 0.002–0.005 $M_\odot$ for the total mass of 2.7 $M_\odot$ with the mass ratio between 0.85 and 1 (Sekiguchi et al. 2016). In this work, we consider the equal-mass merger of 1.35 $M_\odot$ neutron stars, in which the dynamically ejected mass is $\sim 0.002 \, M_\odot$. In contrast to the ejecta mass, the typical velocity and the profile of the electron fraction of the dynamical ejecta
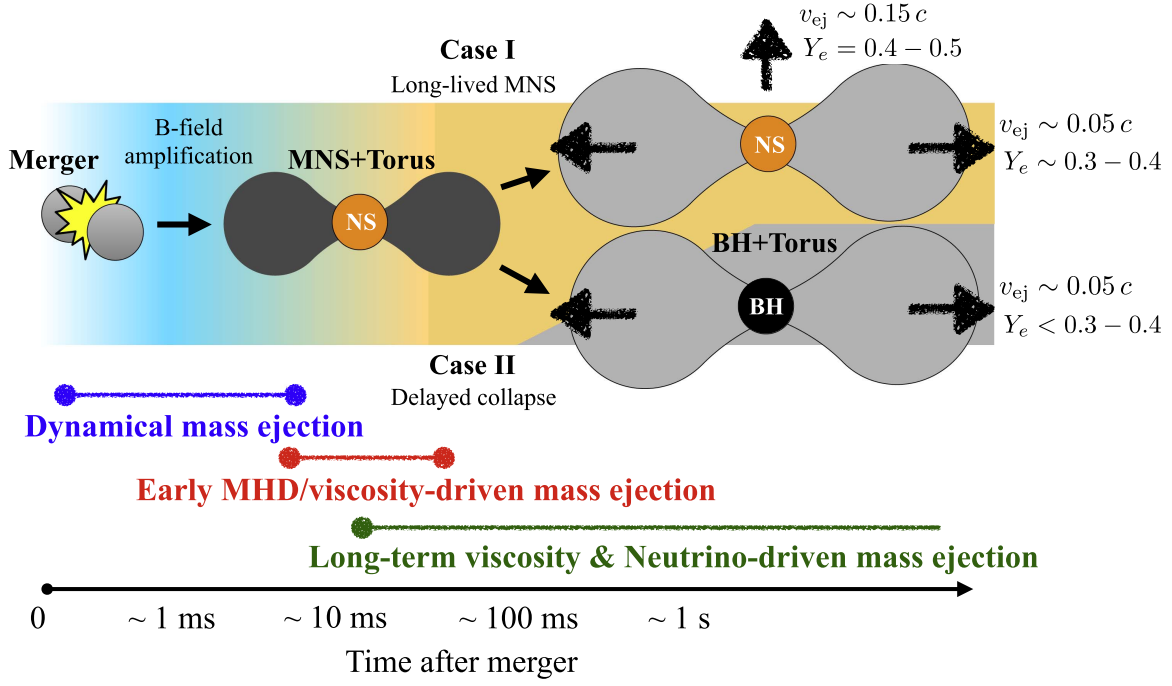
Figure 11. Schematic picture of the overall mass ejection processes in the merger and post-merger phases of binary neutron stars. The time of the delayed collapse of the MNS depends on the neutron star EOS and the total mass of the binary. If the neutron star EOS is stiff enough or the total mass of the binary is small enough, the MNS survives for a long timescale (Case I), at least the timescale of neutrino cooling $\sim$10 s. Otherwise, the MNS collapses to a black hole in the thermal timescale, which is determined by the thermal energy of the MNS and neutrino emission rate, or the timescale for angular momentum transport in the MNS (Case II).

Table 3
Properties of the Ejecta for the DD2 EOS

Type of Ejecta	Mass ($M_\odot$)	V_{ej}/c	Y_e	Direction	Duration
Dynamical ejecta	$O(10^{-3})$	$\sim$0.2	0.05–0.5	$\theta \gtrsim 45°$	$t - t_{\rm merge} \lesssim 10$ ms
Early viscosity-driven ejecta	$\sim 10^{-2}(\alpha_{\rm vis}/0.02)$	$\sim 0.15 - 0.2$	0.2–0.5	$\theta \gtrsim 30°$	$t - t_{\rm merge} \lesssim 0.1$ s
Late-time viscosity-driven ejecta (polar)	$\sim 10^{-3}$ $(t_\nu/{\rm s})$	$\sim$0.15	0.4–0.5[a]	$\theta \lesssim 30°$	$t - t_{\rm merge} \sim t_\nu \sim 10$ s
Late-time viscosity-driven ejecta (equatorial)	$\gtrsim 10^{-2}$	$\sim$0.05	0.3–0.4[a]	$\theta \gtrsim 30°$	$t - t_{\rm merge} \sim 1$–10 s

Note. The table shows the components of ejecta, ejecta mass, average velocity, electron fraction, direction of the mass ejection, and ejection duration. Here t_ν and $t - t_{\rm merge}$ denote the duration of the neutrino emission and the time after the onset of the merger, respectively.
[a] We note that for the EOS in which the value of $M_{\rm max}$ is not as high as that for the DD2 EOS, the MNS could collapse to a black hole within $\sim$1 s. Even for such an EOS, the late-time viscosity-driven mass ejection should continue after the black hole formation, but because of shorter neutrino irradiation time, the value of Y_e is likely to be smaller than 0.3.

depend only weakly on the neutron star EOS, and they are in the ranges 0.15–0.25c and 0.05–0.5, respectively (Sekiguchi et al. 2015).

In the post-merger phase, an MNS surrounded by a torus is typically formed. However, the long-term evolution process of this system depends on the neutron star EOS and total mass of the binary. If the EOS is stiff enough (i.e., the maximum mass for cold spherical neutron stars, $M_{\rm max}$, is high enough) or the total mass of the binary is small enough, the MNS survives for seconds or longer after the onset of the merger as shown in this paper (Case I of Figure 11). Otherwise, the MNS collapses to a black hole after it loses its thermal energy and/or angular momentum (Case II of Figure 11). The time at which the collapse takes place would be determined by the value of $M_{\rm max}$.

The magnetic field strength inside the remnant MNS is likely to be significantly enhanced due to the Kelvin–Helmholtz instability in the shear layer at the onset of the merger (Kiuchi et al. 2015a, 2017). Then, it is natural to suppose that MHD turbulence would be induced, and, consequently, the MHD-driven viscosity is likely to arise. If the lifetime of the MNS is

sufficiently long, i.e., $\gtrsim$ several tens of ms, the early viscosity-driven mass ejection could occur due to an induced sound wave and resulting shock wave generated associated with the variation of the density profile of the MNS caused by the angular momentum transport driven by the MHD turbulence. Our present study indicates that the early viscosity-driven mass ejection proceeds for $\lesssim$0.1 s in a moderately isotropic manner with $\theta \gtrsim 30°$. The mass of this ejecta depends on the magnitude of the turbulent viscosity, but the mass of $\sim$0.01 $M_\odot$ could be ejected for a reasonable value of the viscosity parameter of $\alpha_{\rm vis} = 0.01$–0.04 (Kiuchi et al. 2017). For the fiducial model ($\alpha_{\rm vis} = 0.02$), the mass of the early viscosity-driven ejecta is $\sim$0.01 $M_\odot$. We note that this mass can be larger if the initial torus mass is larger. The typical velocity is in the range 0.15–0.2 c.

The left two panels of Figure 12 show the density and electron fraction profiles of the ejecta at $t = 0.1$ s for $\alpha_{\rm vis} = 0.02$ and 0.04. For both models, the low-electron fraction ejecta exists near the equatorial plane (region 5 in the left panels of Figure 12). This is composed partly of the
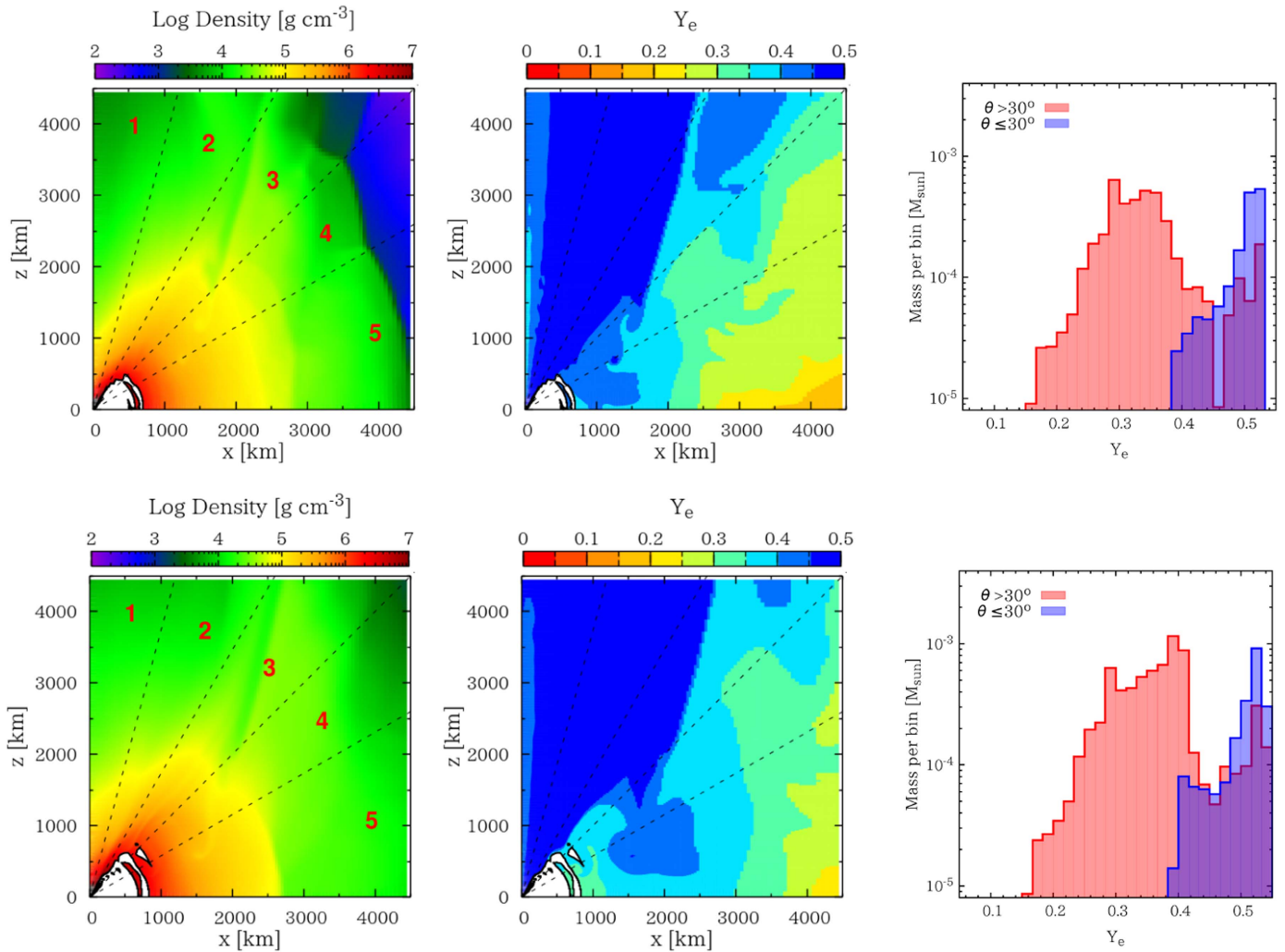
Figure 12. Left panels: snapshots of the density profiles of the ejecta for the models DD2-135135-0.02-H (top) and DD2-135135-0.04-H (bottom) at $t = 0.1$ s. Four black dashed lines and numbers label the five angular regions ($0° \leqslant \theta < 15°$, $15° \leqslant \theta < 30°$, $30° \leqslant \theta < 45°$, $45° \leqslant \theta < 60°$, and $60° \leqslant \theta \leqslant 90°$ with polar angle θ). Middle panels: snapshots of the electron fraction profiles for the same models. Right panels: mass histogram of the ejecta as a function of Y_e for $\theta \leqslant 30°$ and $30° < \theta \leqslant 90°$. Note that the mass histogram is generated for all of the ejecta components calculated by Equation (36).

dynamical ejecta and mainly of the early viscosity-driven ejecta. Since the power for the early viscosity-driven mass ejection is higher for $\alpha_{\rm vis} = 0.04$, the low-electron fraction ejecta is located at a more distant zone for this model. We find that the electron fraction of the early viscosity-driven ejecta is in the range 0.2–0.5 with the peak at $Y_e \sim 0.3$–0.4 (see the right panels of Figure 12).

In the presence of a long-lived MNS, the late-time viscosity-driven mass ejection occurs toward the polar direction for $t \gtrsim 0.2$ s. The top left and middle panels of Figure 13 show the density and electron fraction profiles of this polar ejecta for the fiducial model at $t = 1$ s. The ejecta for $\theta \lesssim 30°$ is launched from the region near the central MNS in assistance with the neutrino irradiation toward the polar direction (regions 1 and 2 in the left panels of Figure 13); hence, the velocity of the ejecta is $\sim 0.15\,c$. Due to the strong neutrino irradiation, the electron fraction of the ejecta is increased to be quite high as 0.4–0.5. The properties of the polar ejecta for the model with $\alpha_{\rm vis} = 0.04$ are similar to those of the ejecta for the fiducial model.

The late-time viscosity-driven mass ejection from the expanded torus occurs as we found for the model with

$\alpha_{\rm vis} = 0.04$ (see the bottom left and middle panels of Figure 13). Even for the lower viscosity parameter models, this type of ejecta is likely to be induced for a later phase, as discussed in Section 3.4. This mass ejection is likely to occur irrespective of the presence of the long-lived MNS, and the velocity of this ejecta is $\sim 0.03 - 0.05\,c$ (Metzger & Fernández 2014). This velocity is appreciably smaller than that for the polar ejecta component because it is launched from the outer region of the torus for which the typical velocity scale is $< 0.1\,c$. In the presence of the long-lived MNS, the effect of the neutrino irradiation is significant enough to increase the electron fraction above ~ 0.3 for this ejecta. The bottom middle panel of Figure 13 shows that the late-time viscosity-driven ejecta is moderately neutron-rich as $Y_e = 0.3$–0.4 for $\theta \gtrsim 30°$. In the absence of the long-lived MNS, the neutrino irradiation is quite minor; hence, the electron faction of the ejecta would be relatively low, as shown by Metzger & Fernández (2014) and Just et al. (2015). Note that for a shorter lifetime of the MNS with $\lesssim 1$ s, the amount of the neutron-rich matter with $Y_e < 0.3$ would be larger than what we found.

Because the mass accretion onto the MNS is significantly suppressed for the late time $t \gtrsim 1$ s, an appreciable fraction of
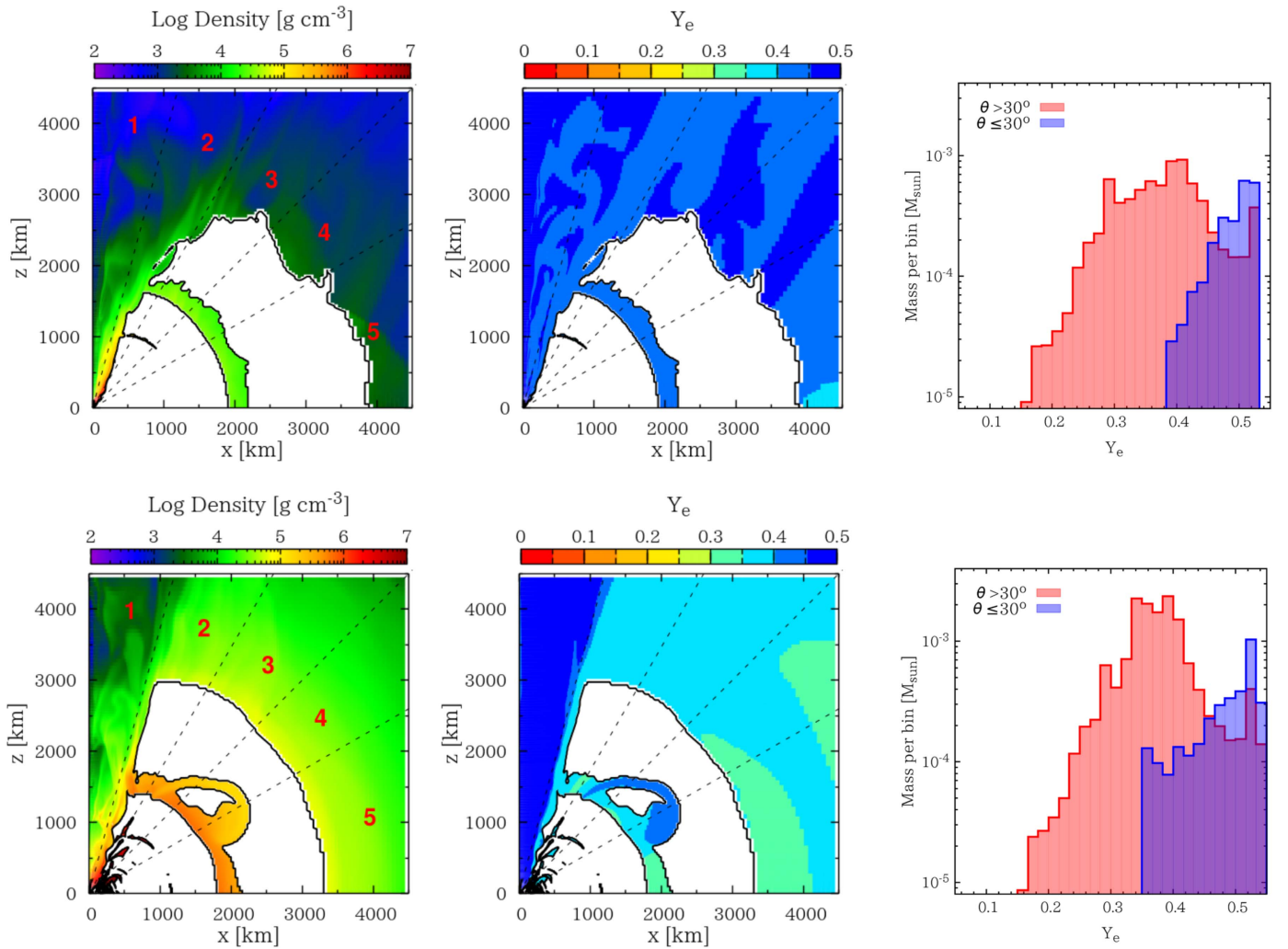
Figure 13. Same as Figure 12 but at $t = 1$ s. For $\alpha_{\rm vis} = 0.02$ (top panels), the ejecta shown in these panels is composed mainly of the viscosity-driven component toward the polar direction, while for $\alpha_{\rm vis} = 0.04$ (bottom panels), it is composed primarily of the viscosity-driven component toward the equatorial direction. In the white region, matter is gravitationally bound ($|hu_t| < 1$).

the torus material is likely to be ejected as the late-time viscosity-driven ejecta. The torus mass for the late time ($t \gtrsim 1$ s) is $\sim 0.05\ M_\odot$ (see the top panel of Figure 4); hence, the mass of this late-time ejecta could be $\sim 0.05\ M_\odot$. We note that this mass can be larger if the initial torus mass is larger.

In Table 3, we summarize the mass, typical velocity, electron fraction, direction of the ejection, and duration for each ejecta component. This is likely to show a universal picture of the mass ejection process from the merger remnant for the case that a long-lived MNS is formed (Case I in Figure 11). On the other hand, if a long-lived MNS is not formed after the merger (Case II in Figure 11), early viscosity-driven ejecta and late-time polar viscosity-driven ejecta would be minor, and the late-time equatorial viscosity-driven ejecta would have a much lower value of Y_e. We also note that if the lifetime of the MNS is shorter than $\lesssim 1$ s, the value of Y_e for the late-time viscosity-driven ejecta could be smaller than 0.3 (Metzger & Fernández 2014; Lippuner et al. 2017).

At the end of this subsection, we emphasize that the viscous hydrodynamics we employ in this work is an effective approach to take into account the angular momentum transport and heating due to the MHD turbulence; hence, the values of the viscosity parameter we assumed in this work should be

justified by performing very high-resolution MHD simulations that resolve a variety of MHD instabilities in the future.

4.2. Elemental Abundance in the Ejecta and Implications for the Electromagnetic Signals

Here we discuss the elemental abundance in the post-merger ejecta. We note that we do not consider the dynamical ejecta in this subsection.

Figure 14 shows the mass histogram of the ejecta as a function of the electron fraction and specific entropy at $t = 1$ s for $\alpha_{\rm vis} = 0.02$ and 0.04. As found in this figure, the electron fraction of the ejecta is widely distributed, but the mass of the ejecta component with $Y_e \lesssim 0.25$ is minor. In this ejecta, it is expected that the r-process elements heavier than the second peak, including lanthanide elements, are not significantly synthesized (e.g., Wanajo et al. 2014; Martin et al. 2015; Tanaka et al. 2018).

Note that the mass histogram of the ejecta for $\alpha_{\rm vis} = 0.04$ exhibits remarkable excess in $Y_e \approx 0.3$–0.4 and $s/k_{\rm B} \lesssim 10$, compared to those for $\alpha_{\rm vis} = 0.02$. The reason for this is that for $\alpha_{\rm vis} = 0.02$, the ejecta at $t = 1$ s is composed mainly of the early viscosity-driven and late-time polar viscosity-driven ejecta, while for $\alpha_{\rm vis} = 0.04$, it is additionally composed of
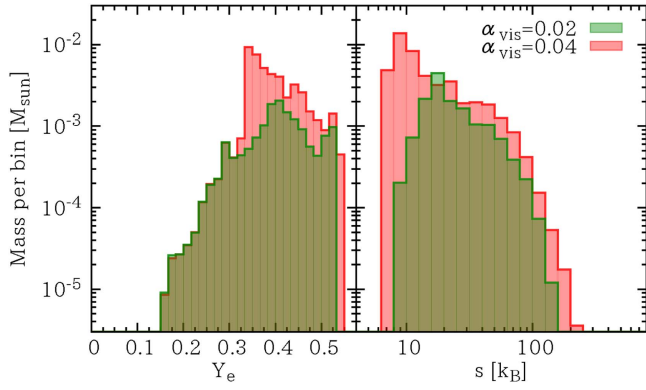
Figure 14. Mass histogram of the ejecta as a function of Y_e (left) and s/k_B (right) at $t = 2.8$ s. The distributions of the electron fraction (left panel) and the specific entropy (right panel) are plotted. The red and green curves denote the results for the models DD2-135135-0.04-H and DD2-135135-0.02-H, respectively.
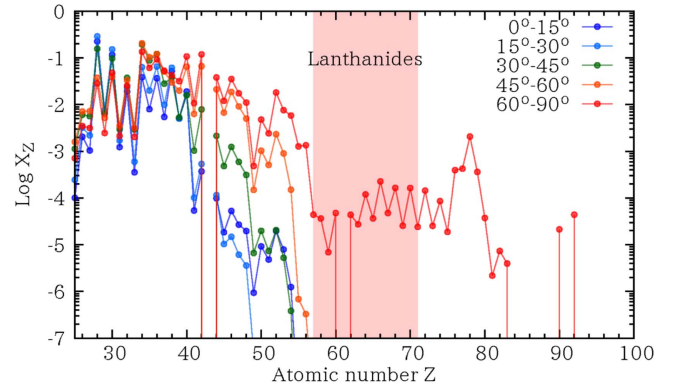

Figure 15. Mass fraction of the nuclei as a function of atomic number for the model DD2-135135-0.04-H at $t = 2.8$ s. The different color curves correspond to the results in different angular regions. The shaded region indicates the range of the lanthanide elements ($Z = 57$–71).

the late-time equatorial viscous-driven ejecta. Thus, the excess found for $\alpha_{\mathrm{vis}} = 0.04$ indicates that the late-time equatorial viscosity-driven ejecta has $Y_e = 0.3$–0.4 and $s/k_B \lesssim 10$.

We performed a nucleosynthesis calculation as a post-process to the ejecta as done in Wanajo et al. (2014). In our scheme, the temporal evolution of temperature, density, and Y_e are obtained by using a tracer particle method (see Nishimura et al. 2015 for details and methodology). In this work, we employed a nuclear reaction network by Nishimura et al. (2016), of which the base theoretical nuclear mass formula is the Finite-Range Droplet Model (FRDM; Möller et al. 1995).

Figure 15 shows the mass fraction of the nuclei as a function of atomic number Z for five angle bins shown in Figures 12 and 13 for the model with $\alpha_{\mathrm{vis}} = 0.04$, in which the late-time equatorial viscosity-driven ejecta is found clearly. As expected from the Y_e histogram, the r-process nucleosynthesis does not proceed sufficiently, and, remarkably, the mass fraction of lanthanide elements is very small. Especially, the material ejected to angular regions 1–4 in Figure 12 (i.e., $\theta < 60°$) is approximately lanthanide-free. In Table 4, the mass fraction of lanthanide and actinide elements in the individual angular regions is shown. We found that the mass fraction is $\lesssim 10^{-7}$ for angular regions 1–4. If the ejecta is contaminated only minorly by the lanthanide elements, the opacity of the ejecta is $\ll 10\,\mathrm{cm^2\,g^{-1}}$ and would be ~ 0.1–$1\,\mathrm{cm^2\,g^{-1}}$ (Tanaka et al. 2018). According to the standard macronova/kilonova model (Li & Paczyński 1998; Metzger et al. 2010), if we observe the post-merger ejecta directly, the time to reach the peak emission, peak luminosity, and its effective temperature are estimated to give

$$t_{\mathrm{peak}} \approx \sqrt{\frac{\kappa M_{\mathrm{ej}}}{4\pi c V_{\mathrm{ej}}}} \xi \approx 1.5\ \mathrm{days} \left(\frac{V_{\mathrm{ej}}}{0.1\,c}\right)^{-1/2}$$
$$\times \left(\frac{M_{\mathrm{ej}}}{0.03\,M_\odot}\right)^{1/2} \left(\frac{\kappa}{0.3\,\mathrm{cm^2\,g^{-1}}}\right)^{1/2} \xi^{1/2}, \quad (42)$$

$$L_{\mathrm{peak}} \approx \frac{f M_{\mathrm{ej}} c^2}{t_{\mathrm{peak}}} \approx 4.3 \times 10^{41} \mathrm{erg\ s^{-1}} \left(\frac{f}{10^{-6}}\right)\left(\frac{V_{\mathrm{ej}}}{0.1\,c}\right)^{1/2}$$
$$\times \left(\frac{M_{\mathrm{ej}}}{0.03\,M_\odot}\right)^{1/2} \left(\frac{\kappa}{0.3\,\mathrm{cm^2\,g^{-1}}}\right)^{-1/2} \xi^{-1/2}, \quad (43)$$

Table 4
Mass Fraction of Lanthanides ($Z = 57$–71) and Actinides ($Z = 83$–103) and Baryon Mass of the Material Ejected for the Angular Regions Shown in Figure 10

Region	$\alpha = 0.04$ ($t = 2.8$ s)		$\alpha = 0.02$ ($t = 3.3$ s)	
	$X_{\mathrm{lan+ac}}$	$M_{\mathrm{ej}}/M_\odot$	$X_{\mathrm{lan+ac}}$	$M_{\mathrm{ej}}/M_\odot$
1	2.1×10^{-10}	0.0031	8.3×10^{-12}	0.0015
2	2.0×10^{-12}	0.0088	9.2×10^{-13}	0.0041
3	1.2×10^{-11}	0.0095	2.3×10^{-11}	0.0038
4	7.1×10^{-8}	0.0089	6.0×10^{-8}	0.0036
5	1.1×10^{-3}	0.0162	1.2×10^{-3}	0.0048
Total	3.8×10^{-4}	0.046	3.1×10^{-4}	0.018

Note. The material ejected by $t = 2.8$ and 3.3 s is analyzed for the $\alpha = 0.04$ and 0.02 models, respectively. The mass fraction of actinide elements is minor compared to that of lanthanides for all angular regions. The actinide mass fraction is less than 10% of that of lanthanide elements even for region 5, where the actinide mass fraction is highest.

$$T_{\mathrm{eff,peak}} \approx \left[\frac{L_{\mathrm{peak}}}{4\pi (V_{\mathrm{ej}} t_{\mathrm{peak}})^2 \sigma_{\mathrm{SB}}}\right]^{1/4} \approx 8 \times 10^3\ \mathrm{K} \left(\frac{f}{10^{-6}}\right)^{1/4}$$
$$\times \left(\frac{V_{\mathrm{ej}}}{0.1\,c}\right)^{1/8} \left(\frac{M_{\mathrm{ej}}}{0.03\,M_\odot}\right)^{-1/8} \left(\frac{\kappa}{0.3\,\mathrm{cm^2\,g^{-1}}}\right)^{-3/8} \xi^{-3/8},$$
$$(44)$$

where f is the radioactive energy deposition factor,[7] κ is the opacity of the material, $\xi\ (\leqslant 1)$ is a geometric factor, and σ_{SB} is the Stefan–Boltzmann constant. Here we suppose that the average velocity is $0.1\,c$. These estimates show that if we observe this post-merger ejecta directly (i.e., from a low opening angle $\theta \lesssim 45°$), the electromagnetic signal would be of a short-timescale, high-luminosity, and blue transient.

We note that in the ejecta component for which $Y_e \gtrsim 0.4$, the nucleosynthesis products are likely to have a smaller heating rate (or smaller value of f). Wanajo et al. (2014) showed that the specific heating rate for the ejecta with $Y_e \gtrsim 0.35$ is much smaller than that of more neutron-rich ejecta. Thus, the high-electron-fraction ejecta may play a minor role as the energy source of the electromagnetic signal (i.e., f could be much

---

[7] We note that f is time-varying and proportional to $\approx t^{-1.3}$ (e.g., Metzger et al. 2010; Hotokezaka et al. 2017).

smaller than 10^{-6}) even if the ejecta mass is much larger than that of the dynamical ejecta. We should also note that Wanajo et al. (2014) considered only dynamical ejecta. The late-time ejecta irradiated by neutrinos has higher entropy than the dynamical ejecta. Even in the high-electron-fraction material, heavy elements can be synthesized if the material has sufficiently high entropy and expansion velocity (see, e.g., Hoffman et al. 1997).

As we found in this paper, the early viscosity-driven ejecta and late-time equatorial viscosity-driven ejecta could have large mass $\gtrsim 0.01\ M_\odot$ and moderately small values of Y_e (0.2–0.5 and 0.3–0.4, respectively). Such ejecta is likely to be the major heating source and contribute to electromagnetic counterparts as the energy source. Note that the mass of the late-time polar viscosity-driven ejecta is likely to be much smaller, and Y_e is large as $\gtrsim 0.4$; hence, their contribution would be minor.

We note that the maximum mass for cold spherical neutron stars for the DD2 EOS is $M_{\rm max} \approx 2.4\ M_\odot$. If the value of $M_{\rm max}$ is not as high as this value for the neutron star EOS in nature, the MNS could collapse into a black hole in a few seconds after the merger. In this case, the electron fraction of the late-time equatorial viscosity-driven ejecta becomes lower than that in the presence of the MNS (Metzger & Fernández 2014; Just et al. 2015; Lippuner et al. 2017); hence, the viscosity-driven ejecta would be more lanthanide-rich. We plan to perform simulations for such an EOS in future work.

4.3. Effects of the Assumptions and Approximations Made in Our Simulations

In our simulation, we make several approximations and assumptions that could affect the results. In Just et al. (2015), the neutrino energy density and flux obtained by the M1 scheme are compared to those calculated by a ray-tracing method for a black hole–torus system. Their result suggests that the neutrino energy density and flux are overestimated by a factor of ≈ 2 in the polar direction (with the polar angle $\theta \lesssim 30°$) and underestimated in the more equatorial direction. In the phase where the neutrino emission from the torus is stronger than that of the MNS, the profile of the neutrino emissivity is nonspherical, so that the neutrino energy density would be overestimated in the polar region, which leads to the overestimation of the neutrino heating rate. Thus, in the earlier phase of the evolution with $t \lesssim 0.5$ s, during which the torus dominates over the whole neutrino emission (see Figure 7), the polar ejecta may be affected by the behavior of the M1 scheme.

However, the outflow launched toward the polar direction is initially slow (see Figure 7 in Fujibayashi et al. 2017), so that the electron fraction of the ejecta in the polar region is settled into an equilibrium value by the neutrino absorption (Qian & Woosley 1996),

$$Y_{e,{\rm eq}} \approx \left(1 + \frac{L_{\bar{\nu}_e}}{L_{\nu_e}} \frac{\epsilon_{\bar{\nu}_e} - 2\Delta}{\epsilon_{\nu_e} + 2\Delta}\right)^{-1}, \qquad (45)$$

where $L_{\nu e}$ and $\epsilon_{\nu e}$ are the luminosity and average energy of electron neutrinos, $L_{\bar{\nu}_e}$ and $\epsilon_{\bar{\nu}_e}$ are those of electron antineutrinos, and $\Delta \approx 1.293$ MeV is the mass difference between neutron and proton. The equilibrium value is unchanged if the ratio of the fluxes of electron neutrinos and antineutrinos and average energy of neutrinos are the same. Thus, the effects of the M1 scheme on the electron fraction of the polar ejecta
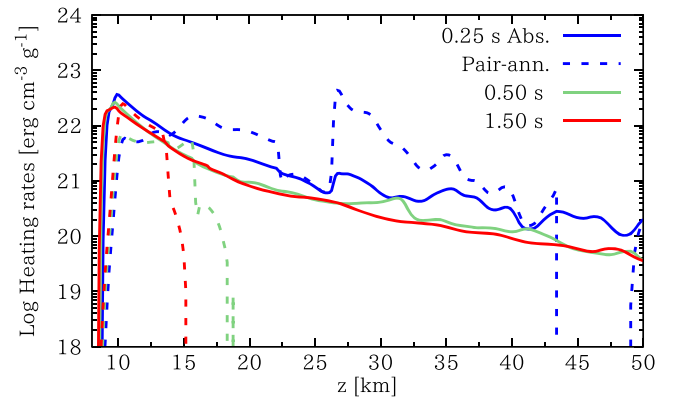

Figure 16. Specific heating rates for neutrino absorption (solid) and pair-annihilation (dashed) processes at $t = 0.25$, 0.5, and 1.5 s.

would be minor if the overestimation of the energy density arises for electron neutrinos and antineutrinos at the same level. On the other hand, in the later phase ($t \gtrsim 0.5$ s), the MNS dominates over the whole neutrino emission of the system; hence, the neutrino emissivity profile becomes more spherical. Thus, the artificial effects due to the M1 scheme would be minor in this phase.

We should note that for the neutrino pair annihilation, the heating rate also depends on the angular distribution of the neutrinos; hence, its heating rate would be affected artificially by the M1 scheme. Figure 16 compares the heating rates due to the neutrino absorption and pair-annihilation processes. While the pair-annihilation heating dominates over the whole heating rate for $t = 0.25$ s, it becomes comparable to the neutrino absorption heating at $z \lesssim 20$ km for later times due to the decrease of the neutrino emission rate. Thus, at least for the early phase ($t \lesssim 0.3$ s), the outflow is primarily powered by the pair-annihilation heating. Pair-annihilation heating has not been considered in most recent works (e.g., Martin et al. 2015; Lippuner et al. 2017). However, the effect could be large, as found here; hence, we need to consider the pair-annihilation heating appropriately to obtain the properties of the ejecta quantitatively.

Since we approximately determine the average energy of neutrinos for calculating the neutrino absorption rates, the uncertainty in the estimated energy would affect the equilibrium value of the electron fraction of the ejecta. If the average energy of neutrinos is higher than that estimated in our simulation, the equilibrium value of the electron fraction becomes lower because the mass difference between neutron and proton becomes unimportant for the higher average energy of neutrinos. Figure 17 shows the average energy of electron-type neutrinos along the rotational axis. This figure shows that the difference between the average energy estimated by Equations (40) and (41) in Fujibayashi et al. (2017) is $\lesssim 50\%$. Using Equation (45), the 50% difference in the average energy around 15 MeV leads to the difference of ≈ 0.06 in the equilibrium value of the electron fraction if the flux of the electron-type neutrinos is the same.

We approximate viscous effects due to MHD turbulence by solving viscous hydrodynamics equations. However, if sufficiently strong magnetic fields are globally formed, the Lorentz force would accelerate the ejecta. This would happen in the polar region because of the low density. The left panel of Figure 10 shows that the density at $z = 20$ km on the rotational
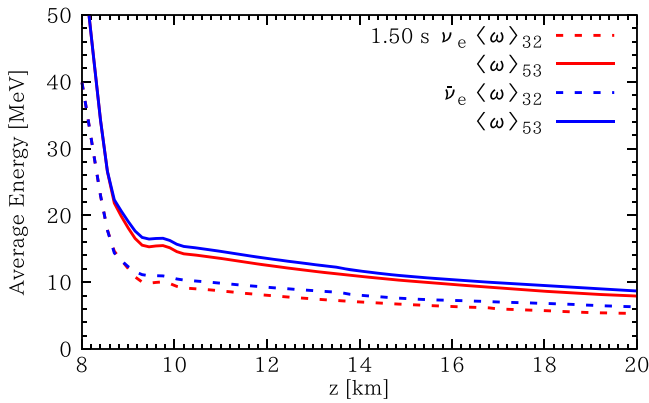
Figure 17. Average energy of electron neutrinos (red) and electron antineutrinos (blue) estimated by Equations (40) and (41) in Fujibayashi et al. (2017; dashed and solid curves, respectively) along the rotational axis at $t = 1.5$ s.

axis is $\approx 10^7 \, \mathrm{g \, cm^{-3}}$, which suggests that the Lorentz force would be important in the region in which the magnetic field strength exceeds 5×10^{14} G. Global magnetic fields could be formed when the outflow is driven because the field line is stretched in the outflow. Such an outflow is driven possibly by the viscous heating and/or neutrino heating. Thus, another ejecta component could be generated as the magnetically accelerated wind from the strongly magnetized MNS. Metzger et al. (2018) suggested that a significant mass ejection ($\gtrsim 0.01 \, M_\odot$) is possible if the MNS is sufficiently magnetized and rapidly rotating. In addition, the density profiles shown in Figure 10 would be modified in the existence of the global magnetic fields (e.g., Metzger et al. 2007 for winds launched from magnetized neutron stars). We should be checking whether global magnetic fields are formed in the relevant timescale after the merger and whether they affect the properties of the ejecta by performing neutrino radiation MHD simulations.

The remnants of binary neutron star mergers have been considered to power relativistic jets that would drive short-duration gamma-ray bursts (Eichler et al. 1989; Nakar 2007). If a relativistic jet is launched from the merger remnant, the jet may inject a part of its kinetic energy into the surrounding ejecta and modify its expansion velocity (cocoon; Murguia-Berthier et al. 2014; Nagakura et al. 2014). Thus, the timescale of the macronova/kilonova emission would be modified to be shorter. The thermal energy in the cocoon injected from the jet would power another component of electromagnetic transient (cocoon emission; Nakar & Piran 2017). Since the post-merger ejecta is lanthanide-poor in our simulation, the timescale of the cocoon emission is likely to be short; hence, this could contribute to the electromagnetic signal in the early phase ($\lesssim$day).

5. Summary

We performed a general relativistic neutrino-radiation-viscous hydrodynamics simulation for a remnant of the binary neutron star merger. Starting from data for a merger remnant obtained from a fully general relativistic merger simulation, we evolved the remnant MNS and torus together. This is the first work in which such a remnant system is evolved in a

self-consistent manner taking into account the effect of angular momentum transport.

We found that there would be two viscous effects on the evolution of the merger remnant. One is the viscous effect on the differentially rotating MNS, which results in the transition of the rotational profile of the remnant MNS from a differentially rotating one to a rigidly rotating one in ~ 10 ms. The other plays an important role in the long-term viscous evolution of the torus.

These viscous effects introduce the mass ejection mechanisms, which do not exist in the inviscid case. As a result of the transition of the MNS density profile due to the redistribution of its angular momentum, a sound wave that becomes a shock wave eventually is formed in the central region, and then the material in the outer region of the torus ($r \sim 100$–1000 km) is ejected by the shock wave for the duration of $\lesssim 0.1$ s. After this early viscosity-driven mass ejection ceases, the late-time viscosity-driven mass ejection takes place from the torus. The mass ejection with neutrino irradiation is activated toward the polar direction first. After the neutrino cooling becomes inefficient in the torus, the viscosity-driven mass ejection from the torus toward the equatorial direction is activated.

Table 3 summarizes the properties of the ejecta by various mass ejection processes. As found from this table, the electron fraction of the post-merger ejecta is distributed between 0.2 and 0.5. In particular, for the polar direction ($\theta < 45°$), the ejecta has higher values of the electron fraction with $Y_e \gtrsim 0.3$. In such ejecta, lanthanide elements are not efficiently synthesized. The dynamical ejecta of the low-electron fraction, which would contain lanthanide elements, is ejected mainly near the equatorial plane. Therefore, if we observe the system from the viewing angle less than 45°, the radioactive emission from the viscosity-driven ejecta does not suffer from the "lanthanide curtain" (Kasen et al. 2015) of the dynamical ejecta, and we will observe a rapid, bright, and blue electromagnetic transient.

This indicates that the electromagnetic emission from the viscosity-driven ejecta could approximately reproduce the electromagnetic signals in the optical–infrared bands associated with GW170817. Our interpretation of these electromagnetic counterparts and further discussion are described in an accompanying paper (Shibata et al. 2017a).

Appendix
Dependency of the Results on the Grid Resolution

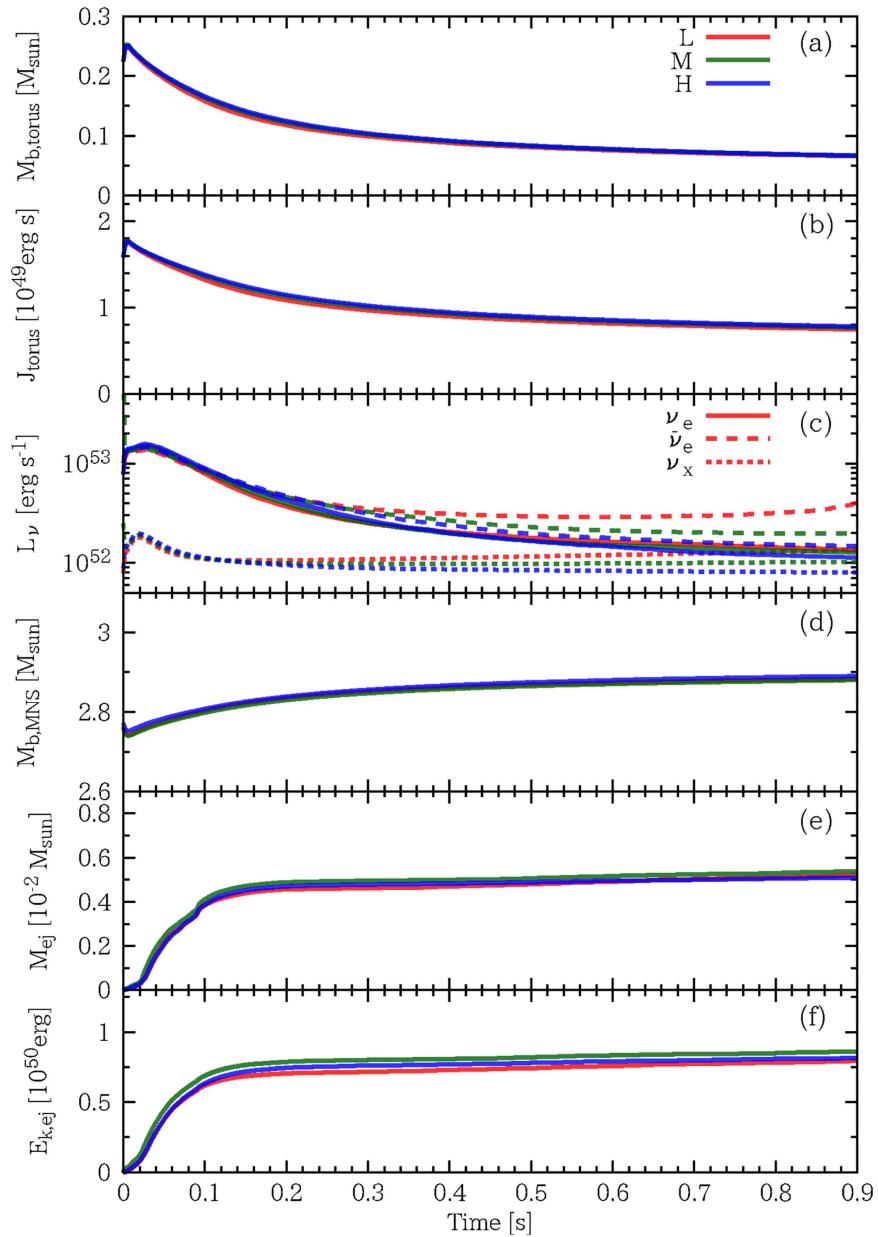In Figure 18, we plot the results for the lower-resolution models DD2-135135-0.01-M and DD2-135135-0.01-L, together

Figure 18. Time evolution of the torus mass (panel (a)), torus angular momentum (panel (b)), neutrino emission rate (panel (c)), baryon mass of the MNS (panel (d)), ejecta mass (panel (e)), and ejecta kinetic energy (panel (f)) for three different resolution models: DD2-135135-0.01-H, DD2-135135-0.01-M, and DD2-135135-0.01-L. In panel (c), the solid, dashed, and dotted curves denote the emission rates of electron neutrinos, electron antineutrinos, and other neutrino species, respectively.

with those for DD2-135135-0.01-H for $\alpha_{\rm vis} = 0.01$. Only for the time evolutions of the emission rates of electron antineutrinos and heavy lepton neutrinos, the agreement with different resolution models becomes poor for the late time, while the agreement with different resolution models is well achieved for the other quantities. This trend is the same as that in the inviscid case, as described in Fujibayashi et al. (2017). A possible reason for this poor behavior is that the density gradient at the surface of the MNS, around which neutrinos are most significantly emitted, becomes steeper for that time; hence, the diffusion process of neutrinos is not accurately resolved with the low resolution. For the $\alpha_{\rm vis} = 0.01$ model, we may conclude that $L_{\bar{\nu}_e} \lesssim 2 \times 10^{52}$ erg s^{-1}, $L_{\nu x} \lesssim 8 \times 10^{51}$ erg s^{-1} at $t = 0.8$ s. We found, from the middle panel of Figure 7, that the emission rate of electron antineutrinos increases for $t \gtrsim 1.2$ s. This behavior also

would be a numerical artifact due to the steep density gradient at the MNS surface for the late phase; hence, the electron fraction of the ejecta would be underestimated because the difference of the emission rates of electron neutrinos and electron antineutrinos would be smaller than that found in our simulation. The differences among the different resolution models at $t = 0.8$ s are within 3%, 4%, 0.3%, 6%, and 8% for the torus mass, torus angular momentum, baryon mass of the MNS, ejecta mass, and ejecta kinetic energy, respectively.

ORCID iDs

Sho Fujibayashi ⓘ https://orcid.org/0000-0001-6467-4969
Kenta Kiuchi ⓘ https://orcid.org/0000-0003-4988-1438
Nobuya Nishimura ⓘ https://orcid.org/0000-0002-0842-7856
Masaru Shibata ⓘ https://orcid.org/0000-0002-4979-5671

References

Abadie, J., Abbott, B. P., Abbott, R., et al. 2010, NIMPA, 624, 223
Abbott, B. P., Abbott, R., Abbott, T. D., et al. 2017a, PhRvL, 119, 161101
Abbott, B. P., Abbott, R., Abbott, T. D., et al. 2017b, ApJL, 848, L12
Accadia, T., Acernese, F., Antonucci, F., et al. 2011, CQGra, 28, 114002
Alcubierre, M., Brügmann, B., Holz, D., et al. 2001, IJMPD, 10, 273
Arcavi, I., Hosseinzadeh, G., Howell, D. A., et al. 2017, Natur, 551, 64
Baker, J. G., Centrella, J., Choi, D.-I., Koppitz, M., & van Meter, J. 2006, PhRvL, 96, 111102
Banik, S., Hempel, M., & Bandyopadhyay, D. 2014, ApJS, 214, 22
Baumgarte, T. W., & Shapiro, S. L. 1999, PhRvD, 59, 024007
Bauswein, A., Goriely, S., & Janka, H.-T. 2013, ApJ, 773, 78
Burrows, A., Reddy, S., & Thompson, T. A. 2006, NuPhA, 777, 356
Campanelli, M., Lousto, C. O., Marronetti, P., & Zlochower, Y. 2006, PhRvL, 96, 111101
Cooperstein, J., van den Horn, L. J., & Baron, E. A. 1986, ApJ, 309, 653
Coulter, D. A., Foley, R. J., Kilpatrick, C. D., et al. 2017, Sci, 358, 1556
Cowperthwaite, P. S., Berger, E., Villar, V. A., et al. 2017, ApJL, 848, L17
Dessart, L., Ott, C. D., Burrows, A., Rosswog, S., & Livne, E. 2009, ApJ, 690, 1681
Drout, M. R., Piro, A. L., Shappee, B. J., et al. 2017, Sci, 358, 1570
Eichler, D., Livio, M., Piran, T., & Schramm, D. N. 1989, Natur, 340, 126
Fernández, R., & Metzger, B. D. 2013, MNRAS, 435, 502
Foucart, F., Haas, R., Duez, M. D., et al. 2016, PhRvD, 93, 044019
Foucart, F., O'Connor, E., Roberts, L., et al. 2015, PhRvD, 91, 124021
Freiburghaus, C., Rosswog, S., & Thielemann, F.-K. 1999, ApJL, 525, L121
Fujibayashi, S., Sekiguchi, Y., Kiuchi, K., & Shibata, M. 2017, ApJ, 846, 114
Fuller, G. M., Fowler, W. A., & Newman, M. J. 1985, ApJ, 293, 1
Goriely, S., Bauswein, A., & Janka, H.-T. 2011, ApJL, 738, L32
Flanagan, É É., & Hinderer, T. 2008, PhRvD, 77, 021502
Hoffman, R. D., Woosley, S. E., & Qian, Y.-Z. 1997, ApJ, 482, 951
Hotokezaka, K., Kiuchi, K., Kyutoku, K., et al. 2013a, PhRvD, 88, 044026
Hotokezaka, K., Kiuchi, K., Kyutoku, K., et al. 2013b, PhRvD, 87, 024001
Hotokezaka, K., Sari, R., & Piran, T. 2017, MNRAS, 468, 91
Israel, W., & Stewart, J. M. 1979, AnPhy, 118, 341
Just, O., Bauswein, A., Pulpillo, R. A., Goriely, S., & Janka, H.-T. 2015, MNRAS, 448, 541
Kasen, D., Badnell, N. R., & Barnes, J. 2013, ApJ, 774, 25
Kasen, D., Fernández, R., & Metzger, B. D. 2015, MNRAS, 450, 1777
Kasliwal, M. M., Nakar, E., Singer, L. P., et al. 2017, Sci, 358, 1559
Kiuchi, K., Cerdá-Durán, P., Kyutoku, K., Sekiguchi, Y., & Shibata, M. 2015a, PhRvD, 92, 124034
Kiuchi, K., Kyutoku, K., Sekiguchi, Y., & Shibata, M. 2017, arXiv:1710.01311
Kiuchi, K., Kyutoku, K., Sekiguchi, Y., Shibata, M., & Wada, T. 2014, PhRvD, 90, 041502
Kiuchi, K., Sekiguchi, Y., Kyutoku, K., et al. 2015b, PhRvD, 92, 064034
Kuroda, K. & LCGT Collaboration 2010, CQGra, 27, 084004
Lattimer, J. M., & Schramm, D. N. 1974, ApJL, 192, L145
Li, L.-X., & Paczyński, B. 1998, ApJL, 507, L59
Lippuner, J., Fernández, R., Roberts, L. F., et al. 2017, MNRAS, 472, 904
Martin, D., Perego, A., Arcones, A., et al. 2015, ApJ, 813, 2
Metzger, B. D., & Fernández, R. 2014, MNRAS, 441, 3444
Metzger, B. D., Martínez-Pinedo, G., Darbha, S., et al. 2010, MNRAS, 406, 2650
Metzger, B. D., Thompson, T. A., & Quataert, E. 2007, ApJ, 659, 561
Metzger, B. D., Thompson, T. A., & Quataert, E. 2018, ApJ, 856, 101
Möller, P., Nix, J. R., Myers, W. D., & Swiatecki, W. J. 1995, ADNDT, 59, 185
Murguia-Berthier, A., Montes, G., Ramirez-Ruiz, E., De Colle, F., & Lee, W. H. 2014, ApJL, 788, L8
Nagakura, H., Hotokezaka, K., Sekiguchi, Y., Shibata, M., & Ioka, K. 2014, ApJL, 784, L28
Nakar, E. 2007, PhR, 442, 166
Nakar, E., & Piran, T. 2017, ApJ, 834, 28
Nicholl, M., Berger, E., Kasen, D., et al. 2017, ApJL, 848, L18
Nishimura, N., Podolyák, Z., Fang, D.-L., & Suzuki, T. 2016, PhLB, 756, 273
Nishimura, N., Takiwaki, T., & Thielemann, F.-K. 2015, ApJ, 810, 109
Perego, A., Rosswog, S., Cabezón, R. M., et al. 2014, MNRAS, 443, 3134
Pian, E., D'Avanzo, P., Benetti, S., et al. 2017, Natur, 551, 67
Qian, Y.-Z., & Woosley, S. E. 1996, ApJ, 471, 331
Radice, D., Galeazzi, F., Lippuner, J., et al. 2016, MNRAS, 460, 3255
Rosswog, S. 2013, RSPTA, 371, 20120272
Ruffert, M., Janka, H.-T., & Schaefer, G. 1996, A&A, 311, 532
Sekiguchi, Y. 2010, PThPh, 124, 331
Sekiguchi, Y., Kiuchi, K., Kyutoku, K., & Shibata, M. 2015, PhRvD, 91, 064059
Sekiguchi, Y., Kiuchi, K., Kyutoku, K., Shibata, M., & Taniguchi, K. 2016, PhRvD, 93, 124046
Shakura, N. I., & Sunyaev, R. A. 1973, A&A, 24, 337
Shappee, B. J., Simon, J. D., Drout, M. R., et al. 2017, Sci, 358, 1574
Shibata, M. 2003, ApJ, 595, 992
Shibata, M., Fujibayashi, S., Hotokezaka, K., et al. 2017a, PhRvD, 96, 123012
Shibata, M., & Kiuchi, K. 2017, PhRvD, 95, 123003
Shibata, M., Kiuchi, K., Sekiguchi, Y., & Suwa, Y. 2011, PThPh, 125, 1255
Shibata, M., Kiuchi, K., & Sekiguchi, Y.-i. 2017b, PhRvD, 95, 083005
Shibata, M., & Nakamura, T. 1995, PhRvD, 52, 5428
Smartt, S. J., Chen, T.-W., Jerkstrand, A., et al. 2017, Natur, 551, 75
Soares-Santos, M., Holz, D. E., Annis, J., et al. 2017, ApJL, 848, L16
Symbalisty, E., & Schramm, D. N. 1982, ApL, 22, 143
Tanaka, M., & Hotokezaka, K. 2013, ApJ, 775, 113
Tanaka, M., Kato, D., Gaigalas, G., et al. 2018, ApJ, 852, 109
Tanaka, M., Utsumi, Y., Mazzali, P. A., et al. 2017, PASJ, 69, 102
Tauris, T. M., Kramer, M., Freire, P. C. C., et al. 2017, ApJ, 846, 170
Timmes, F. X., & Swesty, F. D. 2000, ApJS, 126, 501
Wanajo, S., Sekiguchi, Y., Nishimura, N., et al. 2014, ApJL, 789, L39